

Work started: 1.6.2016
Work submitted for approval: 18.8.2016

HF/MF ray tracing for the Suomi 100 centenary satellite

Mathias Fontell
347501

Instructor: Prof. Esa Kallio
Supervisor: Prof. Esa Kallio

Acceptance

Date ____ . ____ . ____ Grade ____

Accepted by _____

Author: Mathias Fontell

Title: HF/MF ray tracing for the Suomi 100 centenary satellite

Date: 13/11/2016

Language: English

Number of pages: 7+50

Degree programme: Engineering physics

Supervisor: Prof. Esa Kallio

Advisor: Prof. Esa Kallio

In the year 2017, Aalto University is set to launch the Suomi 100 centenary nanosatellite, which is planned to be equipped with an AM HF/MF receiver for studying the Earth's ionosphere and radio propagation. This is intended to be done by computational ray tracing, in which a radio signal is traced through a predetermined medium by sequential refraction and propagation calculations.

In this report we set to describe the basic principles of ray tracing using cold plasma theory and ionospheric physics, and study a variety of published ray tracing methods with their respective results. The insight gained by this study prompted us to develop our own ray tracing software for the Suomi 100 mission, and as a result we propose in this report a numerical Poynting vector method suited for tracing pseudoreal HF/MF rays in a static and anisotropic three-dimensional grid. We also present results of a computer code programmed with the proposed iterative refraction logic, and conclude that the refraction calculations converge with sufficient speed. We ultimately underline known limitations of the proposed ray tracing method, and suggest improvements that are necessary for the Suomi 100 mission.

Keywords: Suomi 100 satellite, ray tracing, radio, ionosphere

Tekijä: Mathias Fontell

Työn nimi: HF/MF ray tracing Suomi 100-satelliitille

Päivämäärä: 13/11/2016

Kieli: Englanti

Sivumäärä: 7+50

Tutkinto-ohjelma: Teknillinen fysiikka

Vastuuopettaja: Prof. Esa Kallio

Ohjaaja: Prof. Esa Kallio

Vuonna 2017 Aalto-yliopiston on tarkoitus laukaista Suomi 100-satavuotisanosatelliitti, joka on suunniteltu varustettavan AM HF/MF-vastaanottimella. Radiovastaanottimella on tarkoitus tutkia Maan ionosfääriä sekä radioaaltojen etenemistä ns. laskennallisen ray tracingin avulla, jossa radiosignaalia seurataan ennaltamääritetyssä väliaineessa peräkkäisten refraktio- ja etenemislaskelmien seurauksena.

Kuvailemme tässä raportissa ray tracingin peruseriaatteet kylmän plasman teoriasta ja ionosfäärifysiikasta lähtien, ja tutkimme erilaisia julkaistuja ray tracing-metodeja sekä niillä saatuja tuloksia. Tästä tutkimustyöstä saatu ymmärrys kannusti meitä kehittämään oma ray tracing-ohjelmamme Suomi 100-tehtävän käyttöön, jonka seurauksena esitämme tässä raportissa numeerisen Poyntingin vektoriin pohjautuvan ray tracing-metodin. Kyseinen metodi soveltuu seuraamaan pseudoreaaleja HF/MF-säteitä staattisessa ja anisotrooppisessa kolmiulotteisessa hilassa. Esitämme myös ehdotetulla refraktiologiikalla ohjelmoidun tietokonekoodin tuloksia, ja huomaamme että kyseiset iteratiiviset refraktiolaskelmat suppenevat riittävällä nopeudella. Lopuksi alleviivaamme ehdotetun ray tracing-metodin tunnetut rajoitteet, ja esittelemme tarvittavia parannuksia Suomi 100-tehtävän toteuttamista varten.

Avainsanat: Suomi 100-satelliitti, ray tracing, radio, ionosfääri

Preface

The work presented in this paper has been carried out at the Department of Radio Science and Engineering at Aalto University School of Electrical Engineering, in the research group for Space Physics during the summer of 2016. The research presented in this paper has been completed in the context of the Finland 100 (Fin: Suomi 100) centenary nanosatellite.

I would like to extend my most sincere gratitude to Professor Esa Kallio, whose expertise and persistence guided my work throughout my time at the Space Physics group. Through his initiative, our group decided to set forth the development of its own ray tracing program, and it is my heartfelt wish that the ray tracer presented in this paper is developed to working condition for the Suomi 100 mission. Moreover, I would like to thank my colleagues and fellow summer students, Petri Koskimaa and Miika Mäkelä, with whom I had the pleasure of working the entire summer. Petri's extensive knowledge of radio technology greatly complemented my theoretical emphasis on radio ray tracing, and Miika's expertise with computational physics helped me considerably with various tasks.

The Suomi 100 nanosatellite is truly a brilliant project for celebrating one century of Finnish independence. The satellite testifies the *zeitgeist* of our dawn in the Space Age, and I should be very grateful for the opportunity to participate in this exciting effort. If everything goes according to plan, the Suomi 100 satellite will be launched to low Earth orbit in late 2017 - from this vantage point, it will provide participating researchers with novel scientific insight, and if all goes well, inspire the space engineers of our future.

Otaniemi, August 18, 2016

Mathias Fontell

Contents

Abstract	ii
Abstract (in Finnish)	iii
Preface	iv
Contents	v
Symbols and abbreviations	vii
1 Introduction	1
2 Background	2
2.1 Cold plasma properties	2
2.2 The terrestrial ionosphere	3
2.3 Electrodynamics and plane waves	5
2.4 Wave propagation in a cold magnetoplasma	7
2.5 The ray	8
2.6 Ray reciprocity and reversibility	11
3 Methods	13
3.1 Ray tracing	13
3.2 Proplab Pro 3	13
3.3 Mars ray tracer	14
3.4 International Reference Ionosphere (IRI)	15
3.5 Ideal magnetic dipole as geomagnetic background	16
3.6 Non-spherical ray tracing grid	16
3.7 Numerical ray tracing method for an anisotropic ionosphere	19
4 Results	24
4.1 Ray path reversibility in Proplab	24
4.2 Effects of collisions in Proplab	26
4.3 Ionospheric profile comparison	27
4.4 Numerical refraction computations	30
4.5 Limitations of the numerical method	33
5 Summary and discussion	35
References	37
Appendix	39
A Cartesian coordinate linear transformations	39
A.1 To plane of incidence	39
A.2 To propagation coordinates	40

A.3 To spherical coordinates	41
B Alternative method for transforming refracted wave normals to the global system	43
B.1 Transmitted wave	43
B.2 Reflected wave	44
C Ray unit vector	45
D Flow chart of the ray refraction algorithm	46
E Multipole expansion of current loop magnetic field	47
F Refractive index argument	49

Symbols and abbreviations

Symbols

e	elementary charge $\approx 1.6022 \times 10^{-19}$ C
c	speed of light in vacuum $\approx 3 \times 10^8$ m/s
ε_0	vacuum permittivity $\approx 8.854 \times 10^{-12}$ F/m
μ_0	vacuum permeability $= 4\pi \times 10^{-7}$ N/A ²
k_B	Boltzmann constant $\approx 1.381 \times 10^{-23}$ J/K
R_E	mean radius of Earth $\approx 6371.0 \times 10^3$ m
\mathbf{E}	electric field [V/m]
\mathbf{B}	magnetic flux density [T]
\mathbf{D}	electric displacement field [Cm ⁻²]
\mathbf{H}	auxiliary magnetic field [A/m]
ρ_f	free electric charge density [Cm ⁻³]
\mathbf{j}_f	free electric current density [Am ⁻²]
N	particle density [1/m ³]
$\hat{\mathbf{u}}$	unit vector of vector \mathbf{u}
\mathbf{u}_\perp	component of vector \mathbf{u} perpendicular to some other vector
\mathbf{u}_\parallel	component of vector \mathbf{u} parallel to some other vector, so that $\mathbf{u} = \mathbf{u}_\perp + \mathbf{u}_\parallel$
$ \mathbf{u} $	Euclidean norm (i.e. length) of vector \mathbf{u}
i	unit imaginary number
\mathbf{k}	wave normal
\mathbf{v}_p	wave phase velocity $= \frac{\omega}{k} \hat{\mathbf{k}}$
\mathbf{v}_g	group velocity $= \frac{\partial \omega}{\partial \mathbf{k}}$

Operators

z^*	complex conjugate of complex number z
$\mathbf{A} \cdot \mathbf{B}$	scalar product of vectors \mathbf{A} and \mathbf{B}
$\mathbf{A} \times \mathbf{B}$	cross product of vectors \mathbf{A} and \mathbf{B}
∇	the nabla operator $= \hat{\mathbf{x}} \frac{\partial}{\partial x} + \hat{\mathbf{y}} \frac{\partial}{\partial y} + \hat{\mathbf{z}} \frac{\partial}{\partial z}$
$\nabla_{\mathbf{r}}$	nabla operator in spatial dimensions
∇f	gradient of scalar field f
$\nabla \cdot \mathbf{A}$	divergence of vector field \mathbf{A}
$\nabla \times \mathbf{A}$	curl of vector field \mathbf{A}
$\frac{d}{dx}$	total derivative with respect to variable x
$\frac{\partial}{\partial x}$	partial derivative with respect to variable x

Abbreviations

AM	A mplitude M odulation
HF	H igh F requencies, i.e. 3 to 30 MHz [3]
MF	M edium F requencies, i.e. 0.3 to 3 MHz
IRI	I nternational R eference I onosphere
UTC	C oordinated U niversal T ime

1 Introduction

In the year 2010, Aalto University (formerly Helsinki University of Technology) began the development of its very own Aalto-1 nanosatellite by offering students of various backgrounds opportunities to participate in the space engineering project. Six years later, Aalto-1 is set to launch to low Earth orbit, thus effectively ushering Finland into the space age. Apart from the novel scientific instrumentation aboard the small nanosatellite, the arguably most valuable gift of Aalto-1 is the experience and inspiration it has granted its participants, both scholarly and professional, since the inception of the project. By the time of this report, the project participants have already founded two companies - ICEYE and Reaktor Space Labs - while many of the students have ventured into other high technology industries.

In late 2017, Aalto University is set to launch the Suomi 100 centenary satellite to celebrate a hundred years of Finnish independence. This nanosatellite, spearheaded by the Aalto Space Physics research group and Professor Esa Kallio, is planned to be fitted with a HF/MF AM radio receiver. Apart from probing near-Earth space weather, the AM radio will be capable of receiving man-made radio transmissions around frequencies of 1-5 MHz. These frequency bands are heavily populated worldwide by both professional and amateur operators alike [8], so the prospect of listening to these transmissions from low Earth orbit can provide interesting insight into ionospheric radio propagation and traffic mapping. The Aalto Space Physics group intends to study this by so-called *ray tracing*, in which the paths of radio signals are numerically computed in a realistic ionospheric background.

The aim of this report is to study the feasibility of numerical ray tracing in the context of Suomi 100, and to present results necessary for the development of our own ray tracing software. This report intends to address the following three areas:

1. Cold plasma theory, and its bearing on ionospheric ray propagation
2. Commercial ray tracing software, such as Proplab Pro 3, and their usability in the context of the Suomi 100 mission
3. Development of our own ray tracing software, and the models required for the purposes of Suomi 100 ray tracing

The development of our own ray tracing software relies on previous work of Rian van Gijlswijk, who formulated a ray tracing program for studying a beacon localization concept on Mars [10]. This background, compounded by commercial ray tracer issues presented in this report, gave us the idea of using our own software for the Suomi 100 mission. However, many different ray tracing methods have been developed for various simplified scenarios, and recognizing limitations of these specific methods is essential for developing a working ray tracer. By performing analysis of cold plasma theory and published results, we intend to propose possible improvements to future versions of our code.

2 Background

2.1 Cold plasma properties

Plasmas are quasineutral gases that consist largely of free ionized particles and electrons. Because plasmas contain a large amount of free charges, they interact strongly with electromagnetic fields in addition to acting as sources for the fields themselves. Cold plasmas, of which the terrestrial ionosphere is a prime example, are of sufficiently low temperature so that thermal effects on wave propagation can be neglected, and cold plasma models generally assume the temperature to be zero. This is because the thermal speeds $\sqrt{2k_B T/m}$ of the plasma particles are much smaller than the phase speeds of the wave phenomena in the plasma [16]. For discussion about the effects of warm plasmas, see [6]. For the Earth's ionosphere, temperature values are typically of the order $\sim 10^3$ K [15].

When a static cold plasma is perturbed, it starts to oscillate at a characteristic frequency known as the *plasma frequency*. Neglecting the smaller oscillatory motion of the greatly more massive ions, the plasma frequency f_p is given in hertz by

$$f_p = \frac{1}{2\pi} \sqrt{\frac{Ne^2}{\epsilon_0 m_e}} \quad (2.1)$$

where N is the plasma electron density and m_e the electron mass.

A single charged particle immersed in a static and homogeneous magnetic field \mathbf{B} is accelerated by the Lorentz force [11], described by the classical equation of motion

$$m \frac{d\mathbf{v}}{dt} = q (\mathbf{v} \times \mathbf{B}). \quad (2.2)$$

Solving equation 2.2 yields a circular cyclotron trajectory around a guiding center, which moves at a constant velocity parallel to the magnetic field lines [16]. The charged particle gyrates around the guiding center at the cyclotron frequency Ω , given in radians per second by

$$\Omega = \frac{|q|B}{m}. \quad (2.3)$$

Since the proton mass is circa 1800 times higher than that of electrons, the cyclotron frequency is consequently around 1800 times higher for electrons.

Another important plasma parameter for wave propagation is the collision frequency ν . Radio waves in the ionosphere undergo some attenuation because the motions of electrons and ions are damped through collisions with neutrals and other charged particles. Throughout the ionosphere, the number density of neutrals is much greater than that of ions. Below about 100 km the collisions between electrons and neutrals dominate, but above this contributions from ions need to be considered as well [6] for ν . Furthermore, the lighter electrons are accelerated significantly more than the heavier ions by the propagating wave, which is why electrons are assumed collide more frequently and thus contribute more into wave attenuation. However, the propagation properties of radio waves are not very sensitive to

the exact value of ν , and in this report we focus mostly on a collisionless ray tracing method.

For future reference, the following plasma parameters are introduced for a plane wave in an 'electrons only' plasma:

$$X = \frac{f_p^2}{f^2}, \quad (2.4)$$

$$Y = \frac{\Omega_e}{\omega} = \frac{\Omega_e}{2\pi f}, \quad (2.5)$$

$$Z = \frac{\nu}{\omega} = \frac{\nu}{2\pi f}, \quad (2.6)$$

$$U = 1 - iZ. \quad (2.7)$$

where the subscript e denotes values for electrons. The angular frequency ω of the plane wave is discussed in chapter 2.3. Some authors, such as Budden [6] and Koskinen [16], give the more general parameter values where ion contributions are allowed for. In this report, we focus on developing a simplified 'electrons only' ray tracing algorithm, but the methods can quite comfortably be extended to include ions as well.

2.2 The terrestrial ionosphere

The terrestrial ionosphere refers to the upper atmosphere of Earth, where solar radiation maintains a significantly high ionization of the otherwise neutral particles. The particles are ionized by photons of the UV range and higher, referred to as photoionization, and energetic particles, referred to as impact ionization. The ionosphere is very dynamic in nature, and the local ionospheric constitution has a strong dependence on solar activity, altitude, time of day and geographic location. The ionosphere has for long been known to significantly affect radio signal propagation, which is why it is imperative to model the ionosphere and its essential characteristics by some means for ray tracing. The prospect of utilizing the International Reference Ionosphere for this purpose is explored in chapter 3.4.

In situ observations with both airborne and ground-based remote sensing instruments have revealed a layered substructure of the terrestrial ionosphere. The ionosphere is thus conventionally divided into three or four regions [23]: The D region (typically below 90 km), the E region (typically between 90 and 130 km) and the F region (above 130 km). The F region is usually divided further into the F_1 and F_2 regions, of which the latter contains the maximum electron density of the ionosphere. The so-called F_2 critical frequency denotes the plasma frequency (Eq. 2.1) corresponding to the maximum electron density of that location. Consequently, the F_2 critical frequency marks the highest possible skywave frequency for near vertical incidence, and helps dictate the maximum usable frequency (MUF) between two transceivers. The F_2 critical frequency ranges between 1-16 MHz, depending on location and time of day, and is usually between 2-5 MHz near Finland. [12]

The collisions between electrons and neutrals in the ionosphere have an effect on radio signal propagation, and introduces damping of the signal amplitude. In this

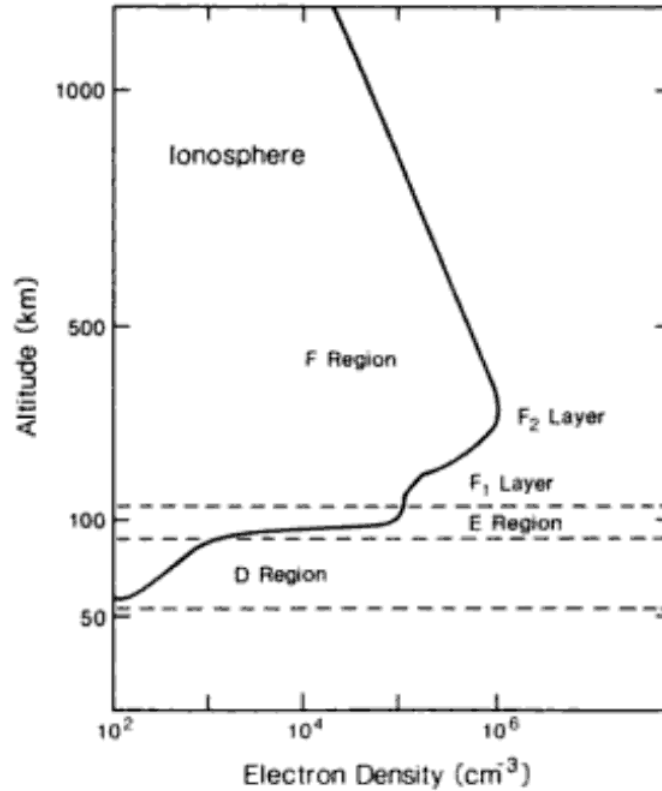


Figure 1: Typical electron density profile of the terrestrial ionosphere as a function of altitude. [15]

report, the effects of ion collisions are neglected. In [23], Schunk and Nagy present the electron-nitrogen and electron-oxygen collision frequency dependencies as given in Equations 2.8-2.9:

$$\nu_{N_2} = 2.33 \times 10^{-17} N_{N_2} (1 - 1.21 \times 10^{-4} T_e) T_e \text{ [Hz]}, \quad (2.8)$$

$$\nu_{O_2} = 1.82 \times 10^{-16} N_{O_2} \left(1 + 3.6 \times 10^{-2} \sqrt{T_e}\right) \sqrt{T_e} \text{ [Hz]}. \quad (2.9)$$

In Eqs. 2.8-2.9 the electron temperatures T_e are given in Kelvin, and the particle densities in m⁻³. For example, using typical ionospheric values of $T_e = 1000$ K, $N_{N_2} = 10^{18}$ m⁻³ and $N_{O_2} = 10^{18}$ m⁻³ at 100 km altitude [12], the neutral collision frequencies are given by

$$\nu_{N_2} \approx 20 \times 10^3 \text{ Hz}, \quad (2.10)$$

$$\nu_{O_2} \approx 12 \times 10^3 \text{ Hz}. \quad (2.11)$$

We attempt to obtain an effective neutral collision frequency ν_{eff} by calculating the weighted average of the collision frequencies as

$$\nu_{eff} = \frac{N_{N_2} \nu_{N_2} + N_{O_2} \nu_{O_2}}{N_{N_2} + N_{O_2}}. \quad (2.12)$$

For the example above, this produces the effective collision frequency

$$\nu_{eff} \approx 16 \times 10^3 \text{ Hz.} \quad (2.13)$$

For 1-5 MHz radio frequencies, inserting this into equation 2.6 yields an estimate for the parameter Z at 100 km altitude

$$Z_{HF/MF} \approx \times 10^{-3}. \quad (2.14)$$

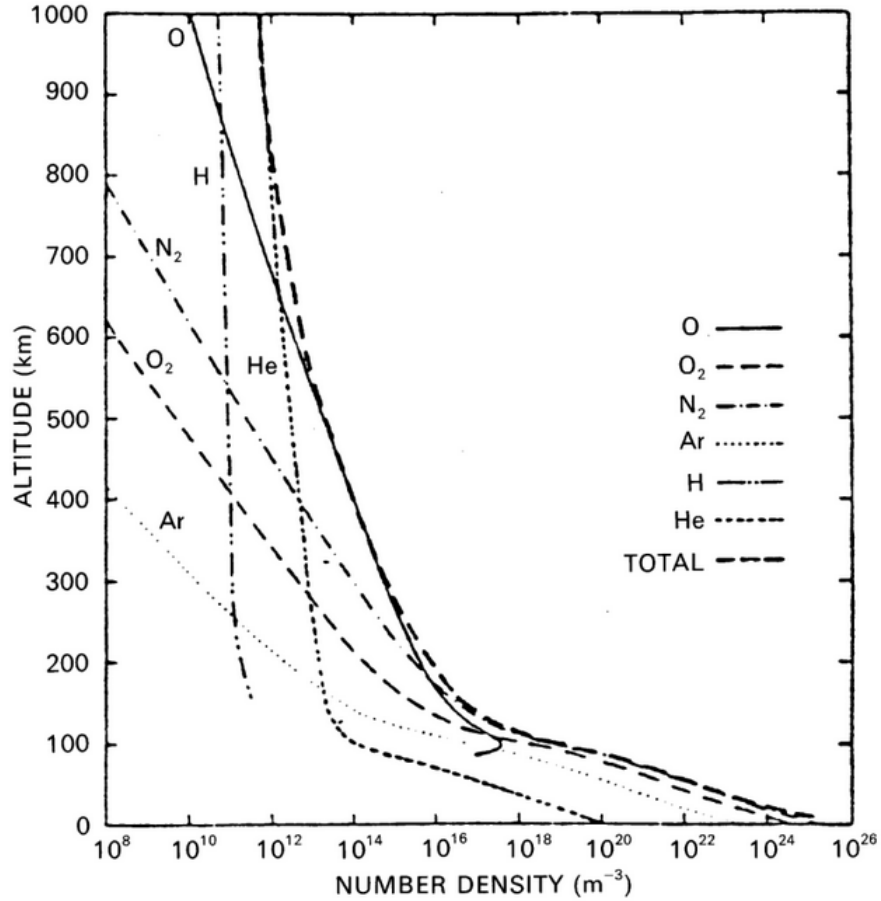


Figure 2: Typical density of neutrals in Earth's ionosphere as a function of altitude. [12]

2.3 Electrodynamics and plane waves

The connection between classical electromagnetic fields and their sources are dictated by Maxwell's equations. When studying the fields in a medium (such as a cold

magnetoplasma), it is useful to present them using the auxiliary fields as [16]

$$\nabla \cdot \mathbf{D} = \rho_f, \quad (2.15)$$

$$\nabla \cdot \mathbf{B} = 0, \quad (2.16)$$

$$\nabla \times \mathbf{E} = -\frac{\partial \mathbf{B}}{\partial t}, \quad (2.17)$$

$$\nabla \times \mathbf{H} = \mathbf{j}_f + \frac{\partial \mathbf{D}}{\partial t}. \quad (2.18)$$

In addition, electric and magnetic fields and their auxiliary fields are linked by the constitutive relations

$$\mathbf{D} = \bar{\epsilon} \mathbf{E}, \quad (2.19)$$

$$\mathbf{B} = \bar{\mu} \mathbf{H}. \quad (2.20)$$

In cold plasma theory, the magnetic permeability $\bar{\mu}$ is usually approximated as being the scalar μ_0 . However, an external magnetic background (such as the geomagnetic field) introduces inevitable anisotropy in the plasma, which manifests itself in the electric permittivity $\bar{\epsilon}$. Hence in an anisotropic plasma, the electric permittivity is generally not a scalar, but a second-order tensor with off-diagonal elements. This anisotropy is accountable for the characteristic wave propagation in a cold plasma, and is of general interest in ray tracing applications. See [6] for an example of permittivity tensor elements.

A steady-state solution to Maxwell's equations without sources is the familiar plane wave solution, which represents a uniform plane propagating in the direction of the wave normal \mathbf{k} with the angular frequency ω :

$$\mathbf{E}(\mathbf{r}, t) = \tilde{\mathbf{E}} e^{i(\mathbf{k} \cdot \mathbf{r} - \omega t)}, \quad (2.21)$$

$$\mathbf{B}(\mathbf{r}, t) = \tilde{\mathbf{B}} e^{i(\mathbf{k} \cdot \mathbf{r} - \omega t)}. \quad (2.22)$$

Here $\tilde{\mathbf{E}}$ and $\tilde{\mathbf{B}}$ are constant complex vectors, and the physical measurable fields are represented by the real parts of Eqs. 2.21-2.22. In the proposed ray tracer, the traced waves are modelled as electromagnetic plane waves, but future versions of the code may include a more physical treatment of antennas in the near/far field. For an overview of antenna radiation in a cold magnetoplasma, see [5].

In a magnetized cold plasma, the plane waves demonstrate rather unintuitive behaviour, and it is prudent to lay out some key characteristics immediately [6]:

- The wave normal \mathbf{k} is real for non-evanescent waves (see chapter 2.4) in a collisionless plasma, but even non-evanescent wave normals \mathbf{k} exhibit an imaginary part if collisions are included. The imaginary part of \mathbf{k} introduce signal attenuation.
- The plane wave fields \mathbf{D} , \mathbf{B} and \mathbf{H} are always pointing perpendicular to the wave normal \mathbf{k} , and are thus always transverse.
- The plane wave electric field \mathbf{E} is also strictly perpendicular (transverse) if the plasma is isotropic, but...

- in an anisotropic plasma, \mathbf{E} is not generally transverse, and may exhibit longitudinal field components.
- The phase velocity \mathbf{v}_p of a cold plasma wave usually exceeds the speed of light, and can even be infinite in some cases.
- However, the group velocity \mathbf{v}_g is never greater than the speed of light.

These properties can be concluded from Maxwell's equations and cold plasma theory, and are demonstrated in [6]. The anisotropic longitudinarity of the electric field has important implications for ray tracing, as consequently the wave group velocity is generally not parallel to the wave normal. Furthermore, including collisions introduces a complex wave normal, and complicates ray tracing significantly. These topics are discussed in chapter 2.5.

2.4 Wave propagation in a cold magnetoplasma

The wave normal number depends, by definition, on the refractive index n as

$$\mathbf{k} = \frac{\omega \mathbf{n}}{c}. \quad (2.23)$$

In a collisional cold magnetoplasma, the complex refractive index is given by the all-important Appleton-Hartree formula (also known as the Appleton-Lassen formula) [6]:

$$n^2 = 1 - \frac{X(U - X)}{U(U - X) - \frac{1}{2}Y^2 \sin^2 \theta + S_R}, \quad (2.24)$$

$$S_R = \pm \left[\frac{1}{4}Y^4 \sin^4 \theta + Y^2 (U - X)^2 \cos^2 \theta \right]^{\frac{1}{2}}. \quad (2.25)$$

Here θ denotes the angle between the wave normal and the background magnetic field \mathbf{B}_0 . The value of the refractive index thus depends not only on the wave frequency, but the wave direction as well. This has an important bearing on refraction calculations, since the angle of refraction cannot subsequently be solved independently of the refractive index.

If n^2 is negative and real, the refractive index n is purely imaginary. This case appears to represent a wave travelling with infinite wave velocity, and is called an 'evanescent' wave. Non-evanescent waves, for which n has a real component, represent propagating waves and are thus of key interest in ray tracing. In lossy media where collisions are included, non-evanescent waves demonstrate complex n with a real component, which represents propagating waves with attenuation [6].

Upon entering the ionosphere, a radio wave will be 'split' into two characteristically polarised magnetoionic wave modes, known as the ordinary (O) and extraordinary (X) modes [4]. In the case of transverse propagation ($\theta = \frac{\pi}{2}$), the O-mode is intuitively understood as a wave whose electric vector is parallel to the magnetic background, while the X-mode exhibits an electric vector perpendicular

to the background. Moreover, for longitudinal propagation ($\theta = 0$ or π) the characteristic modes are known as R- and L-modes [16]. For an arbitrary value of θ , the characteristic modes are defined using the parameter S_R (Eq. 2.25) as follows [6]:

$$\begin{cases} \text{Ordinary (O)} & \text{if } \text{Re}(S_R) > 0, \\ \text{Extraordinary (X)} & \text{if } \text{Re}(S_R) < 0. \end{cases}$$

Our ray tracer should thus trace both the O- and X-modes for a given transmission direction. Although it is possible that the incident wave is polarised so that only one of the characteristic modes is formed, the ray tracer considers both modes by default.

For computing refracted wave directions, one should use the real part of the complex refractive index $\text{Re}(n) = \mu$ (see chapter 3.7). A refraction test code written in C11 incorporates standard libraries for complex arithmetic, which in turn eliminates the need for any analytic expressions for the real and imaginary parts of n .

When a plane wave propagates in an anisotropic plasma, the wave exhibits polarisation characteristic to the corresponding wave mode. Let us use the following Cartesian coordinate system: z is parallel to the wave normal \mathbf{k} , while x and y are perpendicular to propagation. See Appendix A.2 for how the system is defined. In this system, the transverse and longitudinal polarisations are given respectively by [6]:

$$\rho_{\perp} = \frac{E_y}{E_x} = -\frac{H_x}{H_y} = \frac{i\left(\frac{1}{2}Y^2 \sin^2 \theta - S_R\right)}{Y(U - X) \cos \theta}, \quad (2.26)$$

$$\rho_{\parallel} = \frac{E_z}{E_x} = -\rho_{\perp} \frac{iY \sin \theta (n^2 - 1)}{U - X}. \quad (2.27)$$

It is important to notice, that the wave may exhibit a non-zero longitudinal electric field component E_z . This plays a significant role for ray propagation discussed in the next chapter.

2.5 The ray

The energy flux of an electromagnetic field is given by the Poynting vector

$$\mathbf{\Pi} = \mathbf{E} \times \mathbf{H}. \quad (2.28)$$

Let us now evaluate the time average $\mathbf{\Pi}_{\text{av}}$ of the Poynting vector for a progressive plane wave in a cold magnetoplasma. Inserting Eqs. 2.21 and 2.22 into Eq. 2.28, and noting that the real parts of the plane wave fields give the physical fields, the plane wave Poynting vector is given by

$$\mathbf{\Pi} = \text{Re}(\tilde{\mathbf{E}}e^{i(\mathbf{k}\cdot\mathbf{r}-\omega t)}) \times \text{Re}(\tilde{\mathbf{H}}e^{i(\mathbf{k}\cdot\mathbf{r}-\omega t)}) \quad (2.29)$$

$$= \frac{1}{4} \left[\left(\tilde{\mathbf{E}}e^{i(\mathbf{k}\cdot\mathbf{r}-\omega t)} + \tilde{\mathbf{E}}^*e^{-i(\mathbf{k}\cdot\mathbf{r}-\omega t)} \right) \times \left(\tilde{\mathbf{H}}e^{i(\mathbf{k}\cdot\mathbf{r}-\omega t)} + \tilde{\mathbf{H}}^*e^{-i(\mathbf{k}\cdot\mathbf{r}-\omega t)} \right) \right] \quad (2.30)$$

$$= \frac{1}{4} \left[(\tilde{\mathbf{E}} \times \tilde{\mathbf{H}}^*) + (\tilde{\mathbf{E}}^* \times \tilde{\mathbf{H}}) + (\tilde{\mathbf{E}} \times \tilde{\mathbf{H}})e^{2i(\mathbf{k}\cdot\mathbf{r}-\omega t)} + (\tilde{\mathbf{E}}^* \times \tilde{\mathbf{H}}^*)e^{-2i(\mathbf{k}\cdot\mathbf{r}-\omega t)} \right]. \quad (2.31)$$

The last two terms inside the brackets of Eq. 2.31 are oscillatory terms and average zero over an oscillation period. Hence, the remaining two terms give the time-averaged Poynting vector [6]:

$$\mathbf{\Pi}_{\text{av}} = \frac{1}{4}(\tilde{\mathbf{E}} \times \tilde{\mathbf{H}}^* + \tilde{\mathbf{E}}^* \times \tilde{\mathbf{H}}) = \frac{1}{2}Re(\tilde{\mathbf{E}} \times \tilde{\mathbf{H}}^*). \quad (2.32)$$

In a collisionless plasma (i.e. where $Z = 0$), the vector $\mathbf{\Pi}_{\text{av}}$ gives the direction in which a progressive plane wave propagates energy, and is of considerable interest for ionospheric radio applications. The so-called radio *ray* direction is given by the direction of Eq. 2.32 [6]. It is however worth noting, that the ray direction is not necessarily parallel to the wave normal: In free space ($X = 0$) or in an unmagnetized cold plasma ($Y = 0$), the ray vector \mathbf{g} is always in the same direction as \mathbf{k} , but for an anisotropic medium this does not generally hold.

This property can be demonstrated using the polarisation equations presented in chapter 2.4. From the equations for the electric field components, one can observe that in a magnetoplasma the electric field may have a longitudinal component in the direction of the wave normal. This longitudinal component consequently causes the cross product in Eq. 2.32 to exhibit a transverse component perpendicular to wave propagation. The evaluated components of $\mathbf{\Pi}_{\text{av}}$ in a general magnetoplasma (where collisions are allowed for) can be expressed by [6]:

$$\Pi_x = -\frac{iY \sin \theta}{4Z_0} \left[\frac{n\rho_{\perp}^* (n^{*2} - 1)}{U^* - X} - \frac{n^* \rho_{\perp} (n^2 - 1)}{U - X} \right] |E_x|^2, \quad (2.33)$$

$$\Pi_y = \frac{iY \sin \theta \rho_{\perp} \rho_{\perp}^*}{4Z_0} \left[\frac{(n^2 - 1)n^*}{U - X} - \frac{(n^{*2} - 1)n}{U^* - X} \right] |E_x|^2, \quad (2.34)$$

$$\Pi_z = \frac{1}{4Z_0} (n + n^*) (1 + \rho_{\perp} \rho_{\perp}^*) |E_x|^2. \quad (2.35)$$

Here Z_0 denotes the impedance of free space $\approx 376.73 \Omega$. When collisions are neglected (i.e. $U = U^* = 1$), the refractive index n is purely real (or purely imaginary for an evanescent wave). Consequently, the transverse polarisation ρ_{\perp} is purely imaginary. This special case is of interest in our ray tracing program for Suomi 100, as this approximation allows for greatly simplified ray tracing equations. The collisionless components can be written [6]:

$$\Pi_x = \frac{i\rho_{\perp} n(n^2 - 1)Y \sin \theta}{2Z_0(1 - X)} |E_x|^2, \quad (2.36)$$

$$\Pi_y = 0, \quad (2.37)$$

$$\Pi_z = \frac{n}{2Z_0} (1 - \rho_{\perp}^2) |E_x|^2. \quad (2.38)$$

These equations show that the ray is in the plane defined by the Earth's magnetic field, which in the used coordinate system lies in the xz -plane, and the wave normal,

which in the same coordinate system points in the $+z$ -direction (see Appendix A.2). Moreover, in a collisionless plasma, the ray makes an angle α with the wave normal (c.f. Fig. 3):

$$\alpha = \arctan \left[\pm \frac{Y \sin \theta \cos \theta (n^2 - 1)}{\left\{ \frac{1}{4} Y^2 \sin^4 \theta + (1 - X)^2 \cos^2 \theta \right\}^{\frac{1}{2}}} \right] \quad (2.39)$$

where the $+$ sign applies for the ordinary wave and the $-$ sign for the extraordinary wave. The following sign convention is used: α is positive when it is in the same sense as θ , the angle measured from the wave normal to the magnetic field. For further information, see [7] and Appendix C.

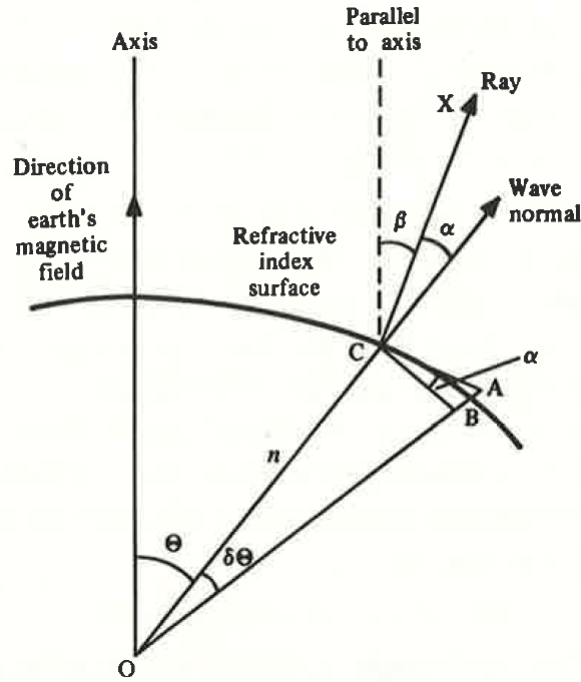


Figure 3: Plane geometric representation of the ray. The angle α denotes the angle between the ray and the wave normal, while β denotes the angle between the ray and the local magnetic field. All three vectors lie in the same plane. [6]

In a lossy medium ($Z \neq 0$) it is necessary to use a complex analogue of $\Pi_{\mathbf{av}}$ that has the same direction as the complex ray. This analogue is given by the bilinear concomitant vector \mathbf{W}

$$\mathbf{W} = \mathbf{E} \times \bar{\mathbf{H}} + \bar{\mathbf{E}} \times \mathbf{H} \quad (2.40)$$

where $\bar{\mathbf{E}}$ and $\bar{\mathbf{H}}$ represent the adjoint fields, given by Altman and Suchy in [2]. For further discussion and theory, refer to [6] and [2]. It is however possible to circumvent the necessity of a complex ray method if the medium is only slightly collisional, in which case it suffices to consider so-called *real pseudo rays*. This is analysed further in chapter 3.6.

2.6 Ray reciprocity and reversibility

The concept of ray path reversibility means, that if a transmitted ray takes a path from A to B, then transmitting an identical ray in the opposite direction from B results in the ray taking an identical path to A [6]. This property is vital to the Suomi 100 mission, because if we intend to conclude transmitter positions by backtracing rays from the satellite, ray reversibility must be assumed. However, physical ray path reversibility is not always true for a cold magnetoplasma, and significant physical breakdown of reversibility is possible in some cases. In this chapter we intend to convince, that for the frequency bands employed by Suomi 100, ray path reversibility should hold to good fidelity.

A related concept to reversibility is reciprocity, which is a more general statement of the electromagnetic fields and their interchangeability in a pair of antennas. In simple terms, if the input current I_1 in antenna A induces the open-circuit voltage V_2 in antenna B, and an input current I_2 equal to I_1 in antenna B induces the same open-circuit voltage $V_1 = V_2$ in antenna A, the pair of antennas are said to be reciprocal [2]. This is expressed more formally by

$$V_1^{o.c.} = V_2^{o.c.} \quad \text{when} \quad I_2(0) = I_1(0). \quad (2.41)$$

Non-reciprocity is common in ionospheric communications, and is caused by plasma anisotropy and polarisations of the antennas. The reciprocity (or non-reciprocity) of the traced rays is however not very interesting in the scope of Suomi 100, as it does not bear significance on the ray tracing study. This is because reversible ray paths may still be non-reciprocal [5] [2].

Most ray tracing models compute ray paths independently from the other ray components, but in the ionosphere it is possible that that the individual components produced at refraction modify one another, essentially creating a coupled system. An overlook of coupled wave equations are presented in [6], where it is argued that this coupling is responsible for ray path non-reversibility. This problem is further studied and demonstrated in [24], which gives examples of computed non-reversible ray paths in a plane-stratified ionosphere when the operating frequency is below the gyrofrequency.

The effects of coupling on reversibility are studied in [24] for frequencies 300-900 kHz, which is well below the operating frequencies of Suomi 100. For 900 kHz, effects of ray path non-reversibility are barely noticeable, as can be seen in Figure 4. It has been argued that the departure from exact reversibility is small in practical cases [24].

These results suggest that the ray paths traced in our code should be reversible, and that ray path reversibility can be assumed for all practical purposes of the mission. It is however completely possible that ray tracing numerics introduces non-physical breakdown of reversibility. For a thorough discourse on reciprocity and reversibility, see [2].

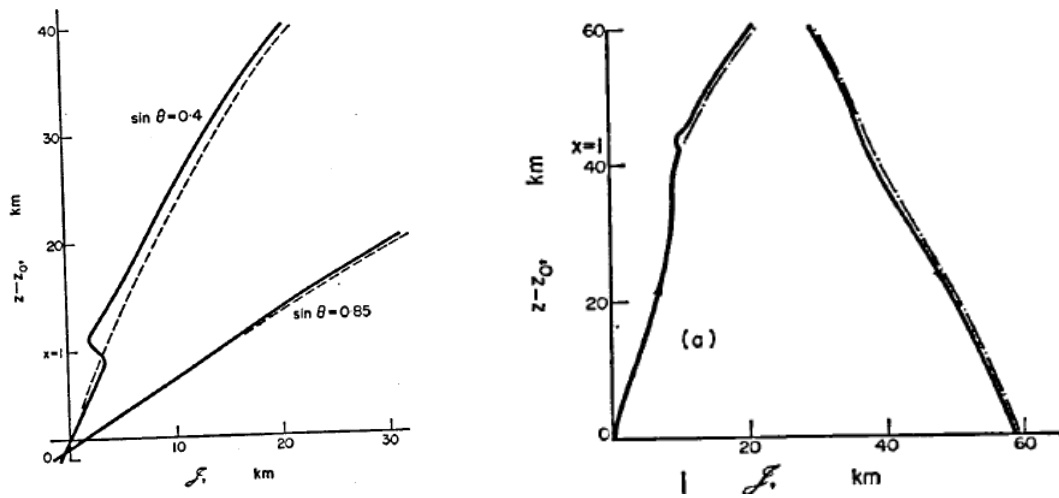


Figure 4: Non-reversible paths for 300 kHz (left) and 900 kHz (right). The continuous curve represents the coupled ray path (non-reversible), while the chain line is the non-coupled (reversible) path. The vertical axis is the ray height, while the horizontal axis represents the horizontal displacement in the plane of incidence for a vertical projection. [24]

3 Methods

3.1 Ray tracing

In physics, ray tracing describes a collection of computational methods in which ray paths are traced in an arbitrary medium of varying propagation characteristics. The subject of ray tracing has several useful applications in varying technologies: For instance in skywave radio communications, ray tracing allows the estimation of usable frequencies and broadcast coverage maps, to name a few. In the context of Suomi 100, the method of radio ray tracing is sought for the purpose of mapping HF/MF radio traffic on Earth: Owing to the approximate reversibility of ray paths, if the satellite receives an AM signal of a known frequency, it is in practice possible to backtrace the ray path to the original sender. Furthermore, an orbital HF/MF receiver enables novel studies into ionospheric physics, and ray tracing between a known transmitter might provide new insight into ionospheric modelling.

In this report, we formulate a numerical Poynting vector method for ray tracing a single frequency in a static, anisotropic three-dimensional discretized grid. The ray tracing equations are not coupled, meaning that the refracted waves propagate independently of one another. For an analysis of coupled wave equations, see [6]. Furthermore, the effects of a small collision frequency ν is accounted for through a pseudo real ray method. The methods described in this report consider an 'electrons only' plasma, but the methods can quite comfortably be extended to include ions as well. Limitations and caveats of the proposed ray tracing methods are presented in chapter 4.5.

3.2 Proplab Pro 3

Proplab Pro version 3 is a commercial radio communication software tool released by Solar Terrestrial Dispatch in the year 2007. Proplab evaluates a three-dimensional worldwide ionosphere from the IRI 2007 model, and is capable of simulating HF/MF radio ray propagation in a geographic simulation domain. For an official overview of Proplab, see [25].

In the context of the work presented in this report, Proplab is studied for three purposes:

1. Evaluate feasibility of using Proplab for ray tracing in Suomi 100.
2. Provide an estimate of ray tracing options that practically affect the performance of our own ray tracer.
3. Serve as a source of code validation for our own ray tracer.

The first item deserves special attention, since the aspect of studying simulated ray path reversibility is enabled by Proplab. Unfortunately, the source code and inner workings of Proplab are not public, leaving any users guessing what the software actually is doing while ray tracing. This 'fatal flaw' is the most significant factor which ultimately led our team to begin the development of our own ray tracing

software for the Suomi 100 project. An original ray tracer would allow its developers to customize the ray tracing equations to desired complexity, and could possibly allow us to test alternative approaches to ray tracing, ionospheric modelling and ionospheric tomography. Nevertheless, one could expect that Proplab accounts for the majority of contemporary ionospheric ray tracing expertise, allowing our team to eventually test our own code by comparing its results to Proplab.

3.3 Mars ray tracer

The predecessor to our Finland100 ray tracer is the 'Mars ray tracer', developed by van Gijlswijk as a part of his Master's thesis on a Mars beacon localization concept [10]. The ray tracer readily executes refraction calculations in a predetermined ionospheric profile, and improving on this program to a more generally applicable version facilitates Suomi 100 ray tracing significantly. Some features and characteristics are presented in Figure 5 with their counterparts in the proposed Suomi 100 ray tracer. Clearly a few modifications to the original Mars ray tracer are necessary. Arguably

Property	Mars ray tracer	Suomi 100 ray tracer
Ionosphere form	Spherically stratified	3D grid
Ionosphere model	Chapman profiles	Manually determined, e.g. IRI 2012 model
Coordinate system	Sun-locked Cartesian	Geographic Cartesian
Magnetic field	No global field	Global dipole field
Refractive index	Real and isotropic at refraction	Complex, anisotropic with collisions
Refraction	Analytic Snell's law	Iterative Snell's law
Ray propagation	Same as wave normal	Not always in direction of wave, pseudo-real
Signal amplitude	Attenuated by collisions along ray path	Attenuated by collisions along ray path

Figure 5: Comparison of the Mars ray tracer and the proposed Suomi 100 ray tracer key properties.

the greatest modifications to the core setup are the global geographic coordinate system and the three-dimensional grid, discussed in chapter 3.6. In terms of refraction physics, the inclusion of a magnetic background is a significant improvement as it introduces realistic anisotropy in the medium. This anisotropy complicates ray tracing somewhat, and the proposed numerical methods are presented in chapter 3.7.

3.4 International Reference Ionosphere (IRI)

The International Reference Ionosphere is an ongoing project with the ultimate ambition of modelling the terrestrial ionosphere to usable precision. The IRI model allows radio operators to predict a realistic ionospheric composition for a certain time and date, which in turn enables simulation of ionospheric radio propagation. The latest version of IRI was released in the year 2012, and is sponsored by the Committee on Space Research (COSPAR) in conjunction with the International Union of Radio Sciences (URSI). For a more detailed overview of IRI, see [17].

IRI provides a handy tool for modelling a feasible ionospheric profile for our Suomi 100 ray tracer. IRI can predict several necessary ionospheric parameters, such as the electron density and temperature as a function of altitude, which subsequently enables the evaluation of the parameters X and Z virtually anywhere in the ionosphere. NASA has developed a web-based tool for computing IRI 2012 parameters, and can be accessed at [28]. For the purposes of this report, a web scraping code programmed in Python 2.7 was created for studying a larger region of IRI predictions. The source code for the program, titled 'IRIscraper 1.0', can be accessed at the Aalto University wiki [1]. The results of such a web scraping over Finland in summertime are presented in chapter 4.3.

While the ray tracer is still in testing before the actual mission, utilizing the web scraping tool is still practical, but when a larger geographic area needs to be covered with sufficient resolution, the web scraping method may become impractical and borderline illegal. The web scraping program sends a large amount of requests to the servers at NASA, and a very intense scraping session could possibly be classified as a form of denial-of-service (DoS). Fortunately, the IRI 2012 model is freely distributed with an available source code in Fortran, which enables any user to compute IRI predictions at their home computer. This alternative is strongly encouraged for future development of the ray tracer, as an embedded IRI-module in the software would allow the ray tracer to cover the entire world at an arbitrarily high resolution.

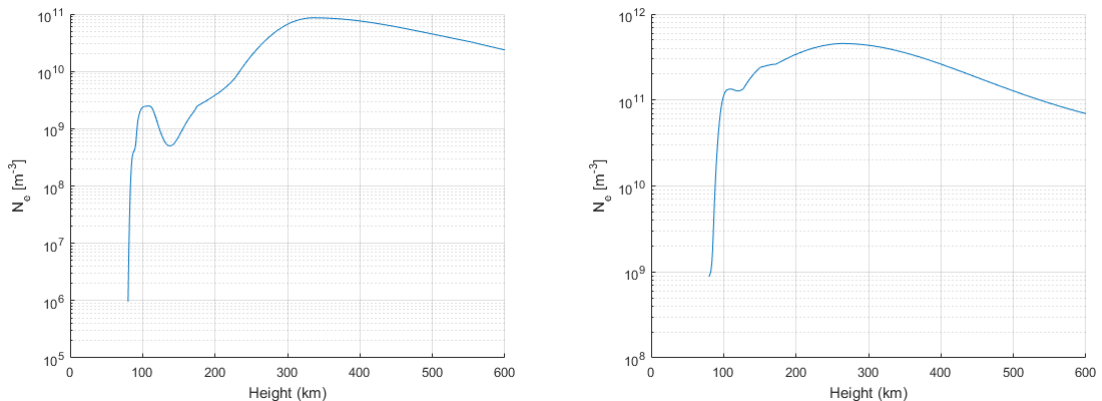


Figure 6: Example of IRI 2012 output of the electron densities as a function of altitude. The profiles were computed near Helsinki at (60°N , 23°E), during midnight in midwinter (left) and midday in midsummer (right). Note the different scales of the vertical axes.

3.5 Ideal magnetic dipole as geomagnetic background

The Earth's intrinsic geomagnetic field is of exceedingly complex nature, and is largely dynamic in both shape, orientation and magnitude. The solar wind interacts with the Earth's magnetosphere, and can cause geomagnetic storm events during which the geomagnetic field is violently perturbed temporarily. For the sake of simplicity, the ray tracer's geomagnetic background is modelled as a static dipole field with constant orientation and magnitude, given by

$$\mathbf{B}_0(\mathbf{r}) = B_0 \left(\frac{R_E}{r} \right)^3 [3(\hat{\mathbf{m}} \cdot \hat{\mathbf{r}}) \hat{\mathbf{r}} - \hat{\mathbf{m}}] \quad (3.1)$$

where B_0 is the mean magnetic field strength at the magnetic equator at $r = R_E$, and $\hat{\mathbf{m}}$ is the magnetic dipole moment unit vector which points towards the South Geomagnetic Pole. See figure 7 for illustration of the magnetic dipole field lines. For derivation of the dipole field, see Appendix E. The NOAA 2015 World Magnetic Model [19] gives the geographic coordinates of the South Geomagnetic Pole as (80.31°S, 107.38°E). This allows us to evaluate the magnetic dipole orientation in the global coordinate system described in chapter 3.6:

$$\hat{\mathbf{m}} = \begin{bmatrix} \hat{x} \\ \hat{y} \\ \hat{z} \end{bmatrix} = \begin{bmatrix} \cos \lambda \cos \psi \\ \cos \lambda \sin \psi \\ \sin \lambda \end{bmatrix} \quad (3.2)$$

$$= \begin{bmatrix} \cos(-80.31^\circ) \cos(107.38^\circ) \\ \cos(-80.31^\circ) \sin(107.38^\circ) \\ \sin(-80.31^\circ) \end{bmatrix} \quad (3.3)$$

$$\approx \begin{bmatrix} -0.05028 \\ 0.16063 \\ -0.98573 \end{bmatrix}. \quad (3.4)$$

B_0 is given slightly different values by varying sources. In [15], Russell gives the approximate value $B_0 \approx 30.4 \mu T$. By using these definitions with equations 3.1 and 2.3, the parameter Y can be determined anywhere in the simulated ionosphere.

3.6 Non-spherical ray tracing grid

For Suomi 100, we attempt to formulate a numerical ray tracing method in a quasi-rectangular three-dimensional grid. The first version of the ray tracer is to consider an 'electrons only' type of plasma, as such a simplification allows most of the physical behaviour to be accounted for. For this model, the grid cells need to be assigned with the following local ionospheric quantities:

1. Electron number density N [m^{-3}]
2. Local magnetic field strength \mathbf{B}_0 due to Earth's dipole field [T]
3. Effective collision frequency ν_{eff} [1/s]

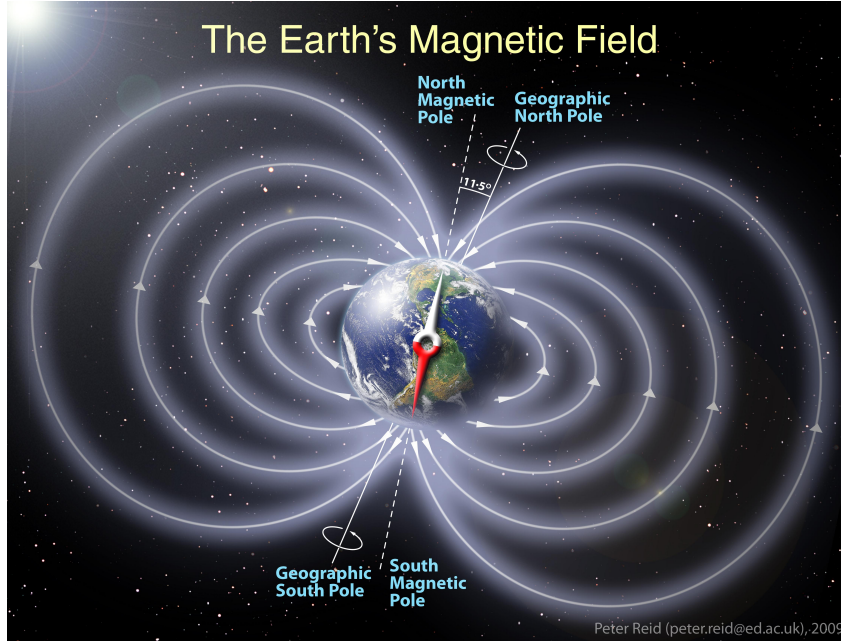


Figure 7: Illustration of Earth's dipole field. [18]

From these, the quantities X , Y and Z can be computed as defined in equations 2.4-2.6, from which the refractive index n can be evaluated for a given wave normal direction.

In the Mars ray tracer developed by van Gijlswijk [10], the global Cartesian coordinate system is oriented so, that positive z points towards the geographic (or in the case of Mars, areographic) North Pole and positive y towards the Sun. For our Suomi 100 ray tracer, this choice of coordinates is not practical if we wish to determine grid cell positions in geographic coordinates (i.e. latitude, longitude and altitude). Thus, we propose that our new ray tracer be programmed with the following coordinate convention, hereafter referred to as *the global (coordinate) system*:

- The origin is placed at the center of the Earth
- The positive z -axis intersects the geographic North Pole (90°N , 0°E)
- The positive x -axis intersects the equator at the Greenwich prime meridian (0°N , 0°E)
- The positive y -axis intersects the equator at the 90th meridian east (0°N , 90°E)

This way the grid cell positions in the global system are determined for a given latitude λ , longitude ψ and altitude h above the surface:

$$\mathbf{r}_{cell} = \begin{bmatrix} x \\ y \\ z \end{bmatrix} = (R_E + h) \begin{bmatrix} \cos \lambda \cos \psi \\ \cos \lambda \sin \psi \\ \sin \lambda \end{bmatrix}. \quad (3.5)$$

The latitudes are defined so that northern latitudes are positive and southern ones are negative. Similarly, eastern longitudes are positive and western ones negative. This way the grid cell positions are given in the same coordinate system as the dipole moment given in in chapter 3.5.

The grid cells are proposed to be stacked in a quasi-rectangular formation, with the top faces pointing radially outward and the side faces pointing in the azimuthal and polar directions. This is illustrated in Figure 8. The simulation domain is to be

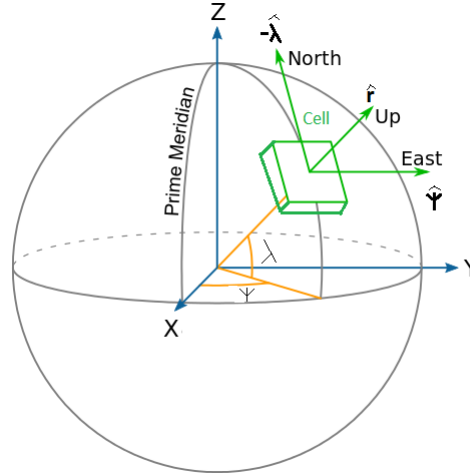


Figure 8: Illustration of the quasi-cuboidal grid cells. The grid cell size is greatly exaggerated. The spherical system vectors discussed in Appendix A.3 are also illustrated in the figure.

determined over a sufficiently large range of geographical coordinates in the vicinity of the satellite. The results of such a grid initialized with IRI electron density values are presented in chapter 4.3, for which a grid was computed over Finland and a specific grid resolution.

For computing refractions, the electron density gradient needs to be calculated numerically from the grid profile. Since the quasi-cuboidal cells are tiled next to one another, the numerical gradient could be evaluated as

$$\nabla_{\mathbf{r}} N = \mathbf{A} \begin{bmatrix} \frac{\partial N}{\partial h} \\ \frac{\partial N}{\partial \zeta} \\ \frac{\partial N}{\partial \chi} \end{bmatrix} \quad (3.6)$$

where \mathbf{A} represents the transformation given in equation A.14. The coordinates h , ζ and χ refer to the spherical altitude and arc coordinates as explained in Appendix A.3. The partial derivatives at a point (h, ζ, χ) could be approximated using a finite

difference method as

$$\frac{\partial N}{\partial h} \approx \frac{N(h + \Delta h, \zeta, \chi) - N(h - \Delta h, \zeta, \chi)}{2\Delta h} \quad (3.7)$$

$$\frac{\partial N}{\partial \zeta} \approx \frac{N(h, \zeta + \Delta \zeta, \chi) - N(h, \zeta - \Delta \zeta, \chi)}{2\Delta \zeta} \quad (3.8)$$

$$\frac{\partial N}{\partial \chi} \approx \frac{N(h, \zeta, \chi + \Delta \chi) - N(h, \zeta, \chi - \Delta \chi)}{2\Delta \chi} \quad (3.9)$$

This method inevitably necessitates some caveats. Since the proposed grid is not strictly rectangular but instead slightly curved, evaluating the numerical gradient by directly applying a finite difference becomes inaccurate if the grid angular resolution is too poor. This is a result of the grid coordinates being actually curvilinear, and has to be accounted for if a more precise numerical gradient is required. Furthermore, the gradient could possibly be assumed to be constant everywhere inside a grid cell, but could alternatively be evaluated for every face of the cell. The latter method might prove more viable due to its intuitive interpretation, but is more complex to implement from a programming point of view.

3.7 Numerical ray tracing method for an anisotropic ionosphere

In an anisotropic and lossless plasma, the wave normal refraction can be solved from the generalized Snell's law, given in [27] by

$$\frac{d}{dP} [\mu \hat{\mathbf{k}}] = \frac{1}{k} \nabla_{\mathbf{r}} \mu \quad (3.10)$$

where P is the phase path and μ the real refractive index. For a Hamiltonian treatment of Eq. 3.10, see [14]. In an anisotropic medium, the refractive index gradient is not precisely parallel to the gradient of N , but in [7] Davies argues that the effect is always less than 10^{-4} radians in the ionosphere. Hence, it can safely be approximated that

$$\nabla_{\mathbf{r}} \mu \parallel \nabla_{\mathbf{r}} N. \quad (3.11)$$

Let's then orient our Cartesian frame so that z is parallel to the boundary normal $\nabla_{\mathbf{r}} N$, while x forms the other vector in the plane of incidence. This transformation to the 'plane of incidence' system is explained in Appendix A.1. Thus, the x-component of the wave unit normal is given by

$$k_x = \sin \gamma \quad (3.12)$$

where γ is the angle between the wave normal and the boundary normal. Since $\frac{\partial N}{\partial x} = \frac{\partial N}{\partial y} = 0$, Equation 3.10 reduces in the x-direction to the familiar form of Snell's law

$$\frac{d}{dP} [\mu \sin \gamma] = 0. \quad (3.13)$$

Equation 3.13 can be used to calculate the direction of the refracted wave normal (or more accurately, the refraction angle):

$$\mu_I \sin \gamma_I = \mu_T \sin \gamma_T. \quad (3.14)$$

Here the subscript I denotes 'incident' and T 'transmitted'. It is worth noting, that Equation 3.14 holds solely for a lossless medium - if losses are included, the refractive index is complex, and subsequently the wave normal is also complex. It was, however, demonstrated in [6] that if the refractive index n only has a small imaginary part, the results with real pseudo rays are still fairly reliable. Equation 3.14 still provides a useful approximation if

$$-\arg(n) = -\arctan\left(\frac{\text{Im}(n)}{\text{Re}(n)}\right) < 10^\circ. \quad (3.15)$$

Moreover, γ_T cannot in general be solved analytically (=independently of μ_T) from equation 3.14 in an anisotropic medium, since the value for the refractive index depends on the angle θ between the wave normal and the magnetic field. For our ray tracer, we propose an iterative method in which the refraction angle is computed recursively until satisfactory convergence is reached. The method is as such: When a ray hits the boundary, the associated wave normal makes an angle γ_I with the boundary normal and has a real refractive index μ_I . The boundary normal is chosen so that it points away from the incident side of the boundary. If total reflection does not occur, an initial guess for the transmission angle is then evaluated as

$$\gamma_{T,0} = \arcsin\left[\frac{\mu_I \sin \gamma_I}{\mu_{T,0}}\right] \quad (3.16)$$

where the initial refractive index is guessed as the isotropic refractive index

$$\mu_{T,0} = \sqrt{1 - X_T}. \quad (3.17)$$

From the transmission angle, the refracted wave normal direction is calculated in the 'plane of incidence' system as

$$\mathbf{k}_{T,i} = \begin{bmatrix} k_{x,T} \\ k_{y,T} \\ k_{z,T} \end{bmatrix} = \begin{bmatrix} \sin \gamma_{T,i} \\ 0 \\ \cos \gamma_{T,i} \end{bmatrix} \quad (3.18)$$

from which the angle θ_T can be calculated from the vector dot product

$$\theta_{T,i} = \arccos\left[\frac{\mathbf{k}_{T,i} \cdot \mathbf{B}_T}{|\mathbf{k}_{T,i}| |\mathbf{B}_T|}\right] = \arccos\left[\frac{\mathbf{k}_{T,i} \cdot \mathbf{B}_T}{|\mathbf{B}_T|}\right]. \quad (3.19)$$

After this, the real refractive index $\mu_{T,i}$ is computed from Eq. 2.24 for $\theta_{T,i}$ and the corresponding propagation mode (X/O) is selected from Eq. 2.25, after which a new iterated value for the transmission angle $\mu_{T,i}$ is evaluated as

$$\gamma_{T,i+1} = \arcsin\left[\frac{\mu_I \sin \gamma_I}{\mu_{T,i}}\right]. \quad (3.20)$$

The next iteration step proceeds with computing a new value for the wave normal (Eq. 3.18). The iteration is stopped once satisfactory convergence is reached. For instance, one could study the relative difference between two consecutive transmission angles

$$\frac{|\gamma_{T,i+1} - \gamma_{T,i}|}{\gamma_{T,i+1}} < \text{tolerance} \quad (3.21)$$

or one could study the numeric error in Snell's law (Eq. 3.14)

$$|\mu_I \sin \gamma_I - \mu_{T,i+1} \sin \gamma_{T,i+1}| < \text{tolerance}. \quad (3.22)$$

As mentioned before, it is possible to achieve total reflection for which no wave is transmitted at refraction. This might be approximated to occur at the limit when $\gamma_T = \frac{\pi}{2}$, and this condition yields the critical angle of incidence γ_I^c

$$\gamma_I^c = \arcsin \left[\frac{\mu_T(\gamma_T = \frac{\pi}{2})}{\mu_I} \right]. \quad (3.23)$$

However, total reflection is not strictly determined by Eq. 3.23 because the refractive index μ_T depends on the transmission angle γ_T . The critical angle γ_I^c should then be sought from the more general condition

$$\gamma_I^c = \arcsin \left[\frac{\max_{\gamma_T} (\mu_T \sin \gamma_T)}{\mu_I} \right]. \quad (3.24)$$

Finding an approximate maximum value $\max_{\gamma_T} (\mu_T \sin \gamma_T)$ could be attempted by simply computing the value of $\mu_T \sin \gamma_T$ for a sufficiently large amount of values in the interval $(0 \leq \gamma_T \leq \frac{\pi}{2})$. Since the sine function $\sin \gamma_I$ is monotonically increasing in the interval $(0 \leq \gamma_I \leq \frac{\pi}{2})$, no solutions to Snell's law (Eq. 3.14) exist for incident angles larger than the critical angle given by Eq. 3.24. Hence, only the reflected wave is formed at total reflection governed by these conditions.

If the incident angle is larger than or equal to γ_I^c , total reflection occurs and the reflected wave is traced. However, the critical angle is not unique for a boundary in an anisotropic plasma, as the incident refractive index depends on the wave direction. The reflection angle γ_R is not generally equal to the incident angle (as opposed to an isotropic medium), and has to be iteratively solved like the transmission angle. Now we use the equations with the incident plasma quantities instead, i.e.

$$\mu_I \sin \gamma_I = \mu_R \sin \gamma_R, \quad (3.25)$$

$$\mathbf{k}_{R,i} = \begin{bmatrix} k_{x,R} \\ k_{y,R} \\ k_{z,R} \end{bmatrix} = \begin{bmatrix} \sin \gamma_{R,i} \\ 0 \\ -\cos \gamma_{R,i} \end{bmatrix} \quad (3.26)$$

$$\theta_{R,i} = \arccos \left[\frac{\mathbf{k}_{R,i} \cdot \mathbf{B}_I}{|\mathbf{k}_{R,i}| |\mathbf{B}_I|} \right] = \arccos \left[\frac{\mathbf{k}_{R,i} \cdot \mathbf{B}_I}{|\mathbf{B}_I|} \right], \quad (3.27)$$

$$\gamma_{R,i+1} = \arcsin \left[\frac{\mu_I \sin \gamma_I}{\mu_{R,i}} \right]. \quad (3.28)$$

In other words, the ray tracer traces the transmitted wave unless total reflection occurs, in which case the reflected wave is traced. It is appropriate to issue certain caveats here. When a wave is refracted in an inhomogeneous plasma, both transmitted and reflected waves are usually formed, but we simply assume the transmitted wave to be more energetic and thus more interesting for ray tracing purposes. It however might happen that the reflected wave has a high amplitude relative to its transmitted counterpart, in which case tracing the reflected wave instead could be justified. Transmission and reflection coefficient matrices for an anisotropic plasma can be found in [6]. The prospect of implementing this feature in future versions of the ray tracer could be considered.

Once the transmitted or reflected wave has been solved, the ray angle α is computed from Equation 2.39 using the real refractive index. Finally, the ray unit vector \mathbf{g} is evaluated as

$$g_x = \left(\frac{\sin \alpha}{\sin \theta} \right) \frac{B_x}{|\mathbf{B}|} + \left(\cos \alpha - \frac{\sin \alpha}{\tan \theta} \right) \frac{k_x}{|k|}, \quad (3.29)$$

$$g_y = \left(\frac{\sin \alpha}{\sin \theta} \right) \frac{B_y}{|\mathbf{B}|} + \left(\cos \alpha - \frac{\sin \alpha}{\tan \theta} \right) \frac{k_y}{|k|}, \quad (3.30)$$

$$g_z = \left(\frac{\sin \alpha}{\sin \theta} \right) \frac{B_z}{|\mathbf{B}|} + \left(\cos \alpha - \frac{\sin \alpha}{\tan \theta} \right) \frac{k_z}{|k|}, \quad (3.31)$$

except for the singular case where the background magnetic field is parallel to the wave normal, in which case the ray and wave normal are consequently parallel:

$$g_x = k_x, \quad (3.32)$$

$$g_y = k_y, \quad (3.33)$$

$$g_z = k_z. \quad (3.34)$$

The derivation of the ray unit vector is presented in Appendix B. The resulting ray is then propagated further until it hits the boundary of the grid cell, and is refracted once more. In order to compute the refraction, it is necessary to transform the magnetic fields into the system defined by the plane of incidence. This transformation is presented in Appendix A.1. The transformation of \mathbf{k} back into the global system is presented in Appendix A.1. The architecture of the ray tracer and refraction logic is clarified in Appendix D.

Results for an implementation of this numeric method (programmed in C11) is presented in chapter 4.4. The aforementioned code, titled 'MatRay 1.0', can be accessed at the Aalto University wiki [1]. The simplifications and approximations used in this ray tracing method inevitably cause some physical ray dynamics to be omitted, at the benefit of faster computation. These inaccuracies and limitations are discussed in chapter 4.5.

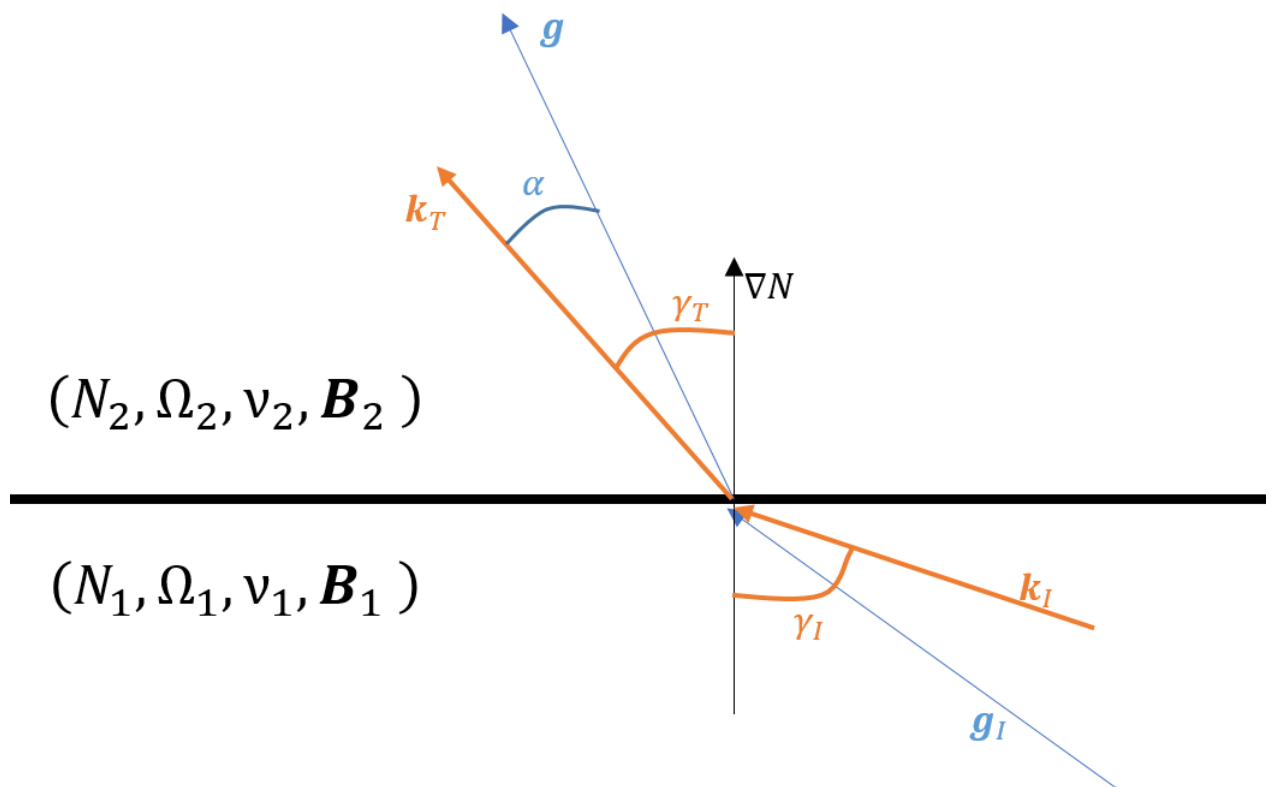


Figure 9: Illustration of refraction at a sharp boundary. The incident ray \mathbf{g}_I hits the boundary at some point of incidence where the outward boundary normal ∇N is evaluated. The transmitted wave normal makes an angle α with the transmitted ray \mathbf{g} . Note that the incident and refracted angles are calculated between the waves and the boundary normal, not between the rays and the boundary normal. Note, that the ray vectors are not necessarily in the plane of incidence.

4 Results

4.1 Ray path reversibility in Proplab

As explained in chapter 2.6, approximate ray path reversibility is implied for non-coupled ray tracing. To better understand how this property behaves in ray tracing software, the following test was performed in Proplab:

1. A transmitter at 400 km altitude above Rovaniemi transmits a radio ray of some frequency, and the transmission direction is fine tuned until the ray hits the receiver in Otaniemi. The test was also done for a transmitter above Oslo.
2. The test is done for frequencies between 1-10 MHz.
3. The received ray direction is reversed, and transmitted from Otaniemi towards the original transmitter
4. The test is performed for two extreme scenarios: Midday in midsummer (21.6.2015 11:00 UTC) and midnight in midwinter (21.12.2015 00:00 UTC).

These transmitter positions were chosen because they are sufficiently close to Otaniemi, and allow different propagation directions with respect to the magnetic background.

Some results for wintertime between Rovaniemi and Otaniemi are presented in Figures 10 and 11. It can be seen that a high enough frequency is reversible, but when the frequency becomes low enough the ray path is no longer reversible. For the shown scenarios, the F_2 critical frequency is around 2 MHz. In summertime, non-reversibility occurs below 7 MHz. The most conspicuous feature of this non-reversibility is that it also happens for an entirely non-collisional and isotropic model: Including anisotropy and collisions only slightly changes the non-reversible frequencies. The fact that Proplab ray paths are non-reversible even for an isotropic plasma raises many questions about its ray tracing algorithms, and leads to suspicion that the observed non-reversibility is caused by numerics rather than physics. Without any clues to the actual equations and models used by Proplab, this non-reversibility is completely inexplicable. These results suggest, that Proplab is not the best alternative for Suomi 100 ray tracing, as it provides no explanations and verifiability for its results.

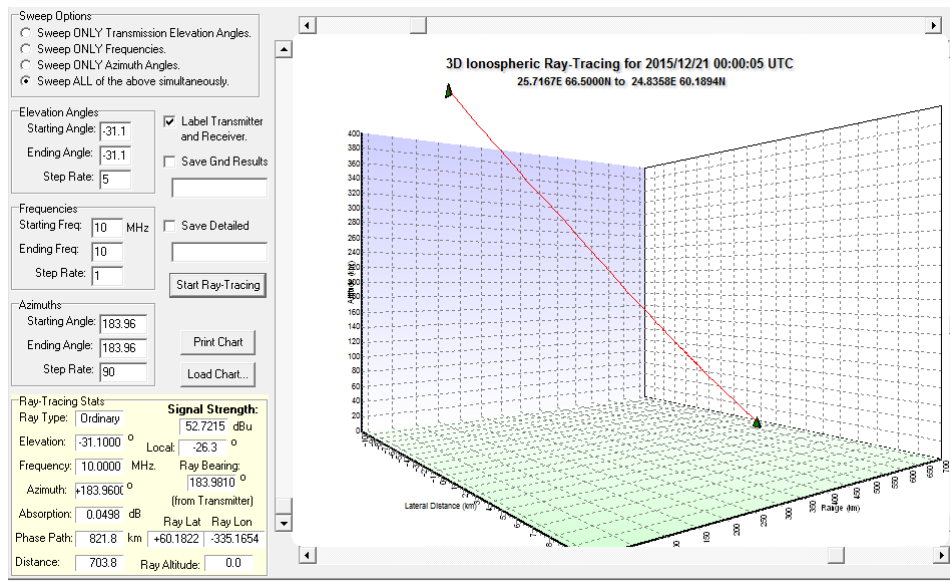


Figure 10: Ordinary ray reversibility test in midwinter for a magnetic and collisional plasma with the Proplab Pro 3 software. The 10 MHz transmission to Otaniemi traces a path to the receiver, and the reverse transmission (i.e. in the exact opposite direction) from Otaniemi takes the same path to the satellite. The reverse path is not shown in the figure due to indistinguishable proximity.

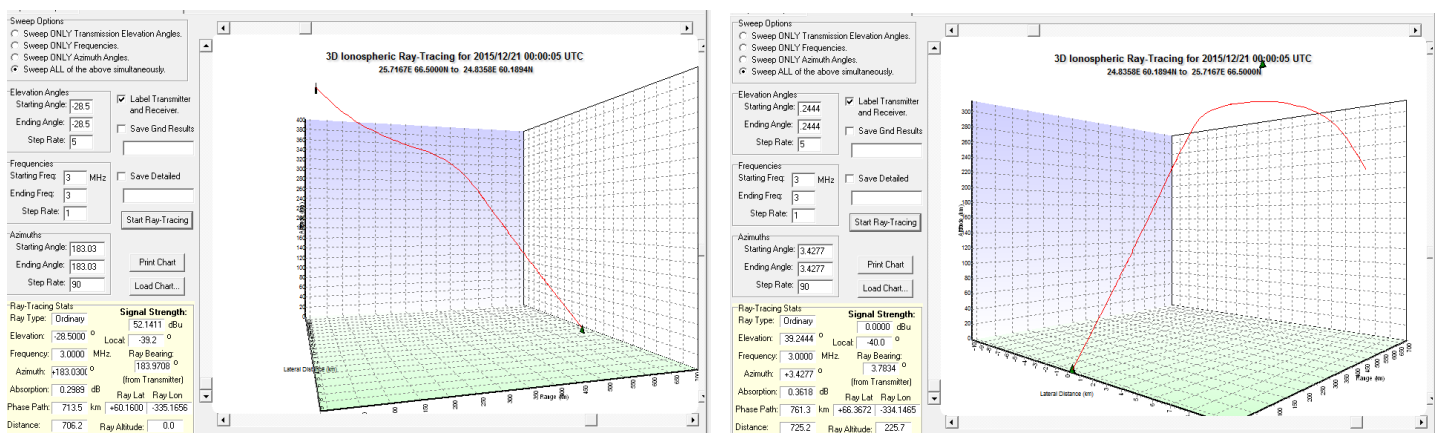


Figure 11: Ordinary ray reversibility test in midwinter for a magnetic and collisional plasma with the Proplab Pro 3 software. The 3 MHz transmission from the satellite 400 km above Rovaniemi (left) traces a path to the ground station receiver in Otaniemi, but the reverse transmission from Otaniemi to the satellite above Rovaniemi (right) diverges from the reversible path at 300 km altitude and misses the original transmitter by several 10 km. Instead of penetrating the ionosphere and reaching the satellite, the transmission is reflected at some 300 km altitude back towards the ground, as can be seen in the figure to the right.

4.2 Effects of collisions in Proplab

It was decided to study the effects of collisions in Proplab, as it could provide practical insight into the reliability of the pseudo-real ray method proposed for our own ray tracer. Proplab allows the user to include (or exclude) both collisions and anisotropy from ray tracing computations, and although it is unclear how Proplab in practice accounts for collisions, we expect that the used models allow for a preliminary study of the methods proposed in this report.

For studying the effects of collisions, a test was devised in which a ray was transmitted from Rovaniemi to Otaniemi using two dispersion models: Appleton-Hartree with field and without collisions, and Appleton-Hartree with field and with collisions. The test was done on 21.12.2015 00:00 UTC, for which IRI predicts a 2 MHz F_2 average critical frequency. The results are shown for 5 MHz and 3 MHz rays in Figure 12.

Ordinary mode		No collisions	With collisions	Extraordinary mode		No collisions	With collisions
5 MHz	Elevation [deg]	-28.5	-28.5	5 MHz	Elevation [deg]	-27.0	-27.0
	Bearing [deg]	183.30	183.30		Bearing [deg]	183.10	183.10
3 MHz	Elevation [deg]	-26.7	-26.7	3 MHz	Elevation [deg]	-32.78	-32.78
	Bearing [deg]	180.32	180.32		Bearing [deg]	172.89	172.89

Figure 12: Comparison of collisional and non-collisional ray tracing in Proplab on 21.12.2015 00:00 UTC. The ray was transmitted from Rovaniemi at 400 km altitude in the given direction (elevation and bearing) by finding a direction so that the ray traced a path to Otaniemi. Ionosphere anisotropy was included in all ray tracings.

These results suggest that ionospheric collisions have a very small bearing on the ray path, as is evidenced by the transmission directions being equal in both cases. In chapter 2.2 it was argued that the parameter Z (Eq. 2.6) is at largest around magnitude 10^{-3} , further suggesting that the refractive index is mostly real for ground-to-satellite transmissions. Although collisions seem to be negligible for transmissions between Rovaniemi and Otaniemi, it might occur that transmissions between another pair of transmitters experience significant ray path differences when collisions are included. For instance, at lower latitudes the ionospheric collisions frequencies are expected to be higher due to higher electron temperatures, which might in turn result in a more imaginary refractive index.

Testing collisions contributions in a wider range of scenarios for 1-5 MHz is not straightforward, because such low frequencies become evanescent in a thick ionosphere. It should be considered to conduct a thorough analysis on how the refractive index is affected by a realistic collision profile. This could be done by predetermining an altitude profile for electron density, temperature and neutral density, and computing the resulting altitude profile for the refractive index n when $Y=0$. By excluding the background magnetic field, n is independent of the specific wave direction, which would in turn allow one to determine an approximate refractive index at any altitude without specifying any transmissions. Summa summarum, the

acquired results suggest that the proposed pseudo-real ray tracing method should be pursued further for the Suomi 100 mission.

4.3 Ionospheric profile comparison

The three-dimensional properties of the ionosphere were studied by sweeping IRI altitude profiles over a range of longitudes and latitudes, during 21.07.2016 16:00 UTC. The sweeping was done from (60°N, 20°E) to (70°N, 30°E) with a 1° resolution in both longitudinal and latitudinal direction. Electron densities were requested as an altitude profile, ranging from 80 to 400 km with a 1 kilometer resolution. This way, a profile for the IRI-predicted ionosphere directly above Finland was obtained. The profiles were acquired by web scraping the web-based IRI 2012 model [28], and writing the results to an ASCII text file for later analysis. A screenshot of the web scraping program is presented in figure 13.

The screenshot shows the IRIscrapper LOOP application window. It contains the following settings:

SETTINGS:					
Year	2016	Coordinate Type	Geographic	Start height [km]	80
Month	7	Start latitude [deg]	60.0	Stop height [km]	400
Day	21	Start longitude [deg]	20.0	Height step [km]	1
Time	Universal	Stop latitude	70.0	Latitude step [deg]	1
Hour of day	16	Stop longitude	30.0	Longitude step [deg]	1

IRI MODEL OPTIONS:					
Sunspot number, Rz12	0.0	Ionospheric index, IG12	0.0	Get values from web (uses time in settings)	
F10.7 flux, daily	0.0	F10.7 flux, 81-day	0.0		
Ne Topside	IRI01-corr	F peak model	URSI	foF2 storm model	on
Bottomside Thickness	ABT-2009	F1 occurrence probability	Scotto-1997 with L	Ne D-region	IRI-95
Auroral boundary	off	foE auroral storm model	off		
Te Topside	TBT-2012	Ion Composition	RBV10/TTS03		

At the bottom, there is a green 'EXECUTE' button and a status indicator 'Awaiting command...'.

Figure 13: Screenshot of the IRI web scraping program’s user interface, and the settings used for the data presented in this chapter.

Results of the 3D analysis using Matlab R2016 are presented below. Figures 14 and 15 show that the IRI-predicted ionosphere is not homogeneous at any altitude, demonstrating that the ionosphere is not spherically stratified. Figure 16 demonstrates some conspicuous three-dimensional properties of the IRI-predicted ionosphere, namely that the density gradients (which are normal to the isosurfaces) can be locally horizontal. This is evidenced by the folded isosurface to the right in figure 16. However, as can be seen from figure 6, the density profiles can vary strongly with altitude and locally exhibit significant radial gradients.

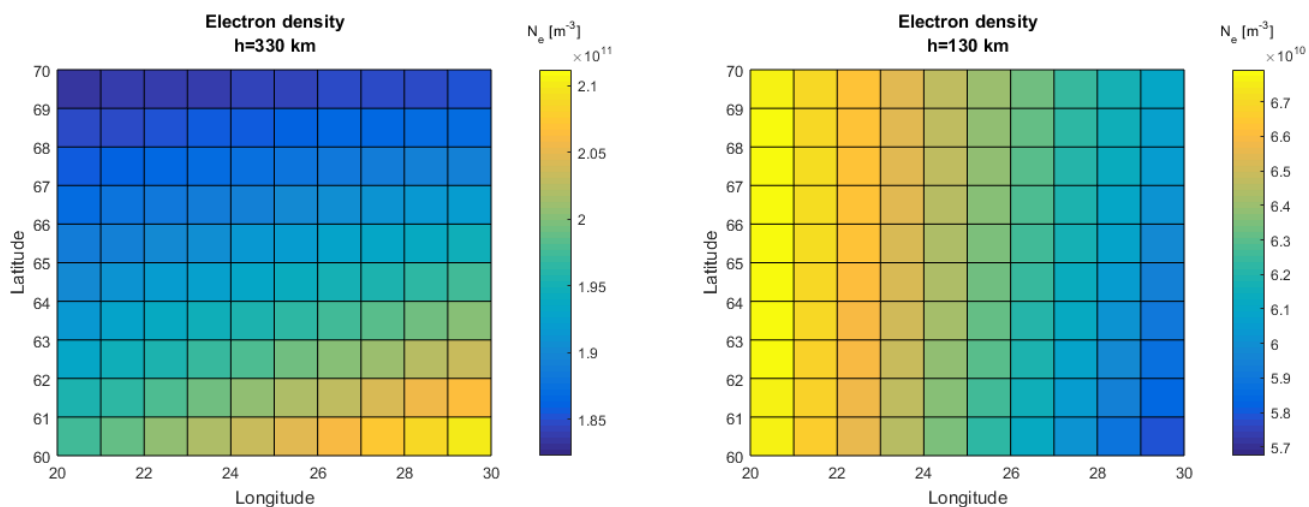


Figure 14: Surface plots of the electron density at altitudes 330 km (left) and 130 km (right), on July 21 2016 16:00 UTC as given by the IRI 2012 model.

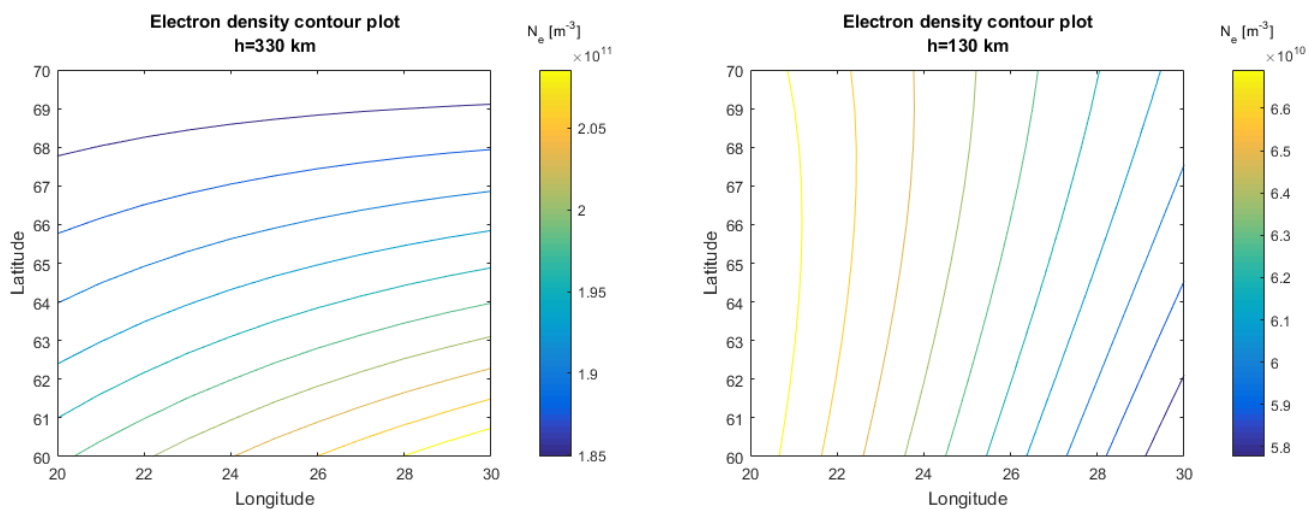


Figure 15: Isocontour plots of the electron density at altitudes 330 km (left) and 130 km (right), on July 21 2016 16:00 UTC as given by the IRI 2012 model.

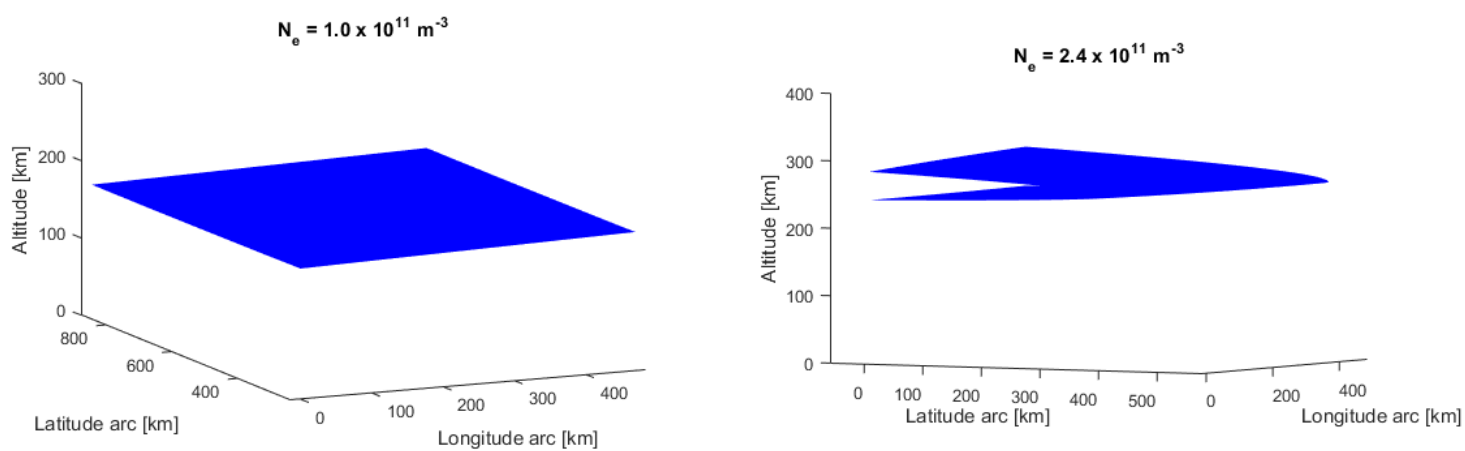


Figure 16: Isosurface plots of the electron density for $1.0 \times 10^{11} \text{ m}^{-3}$ (left) and $2.4 \times 10^{11} \text{ m}^{-3}$ (right), on July 21 2016 16:00 UTC as given by the IRI 2012 model. The longitude and latitude arcs represent the geographic displacements along the surface. All axes are scaled equally.

4.4 Numerical refraction computations

In this chapter we study the results for an implementation of the numerical ray refraction method presented in chapter 3.7. The code programmed in C11 computes the ray direction after a single boundary refraction event, where the quantities X , Y , Z and \mathbf{B}_0 directions are predetermined for both sides of the boundary. An incident wave normal \mathbf{k}_I and boundary normal ∇N are given in an arbitrary Cartesian system, after which the program follows the refraction logic presented in Appendix D to compute the ray unit vector \mathbf{g}_2 after refraction.

For the first test, convergence of the numerical method was studied in an anisotropic and collisionless medium. The transmission side parameters (denoted by the subscript 2), \mathbf{k}_I and ∇N were initialized as presented in table 1. Refraction was tested then for both O- and X-waves, and for incident refractive indices of 1.0 (=free space), 0.5 (=thick layer of ionosphere) and 0.1 (=very thick layer of ionosphere). All waves were incident at a 45° angle. The vector $\mathbf{B}_{0,2}$ was chosen to promote non-transverse propagation of the waves, thus complicating refraction iteration.

X_2	Y_2	Z_2	$\mathbf{B}_{0,2}$	\mathbf{k}_I	∇N
0.3139	0.2799	0	(1, 1, 1)	(1, 0, 1)	(0, 0, 1)

Table 1: Parameters used in collisionless refraction analysis.

The stopping conditions of the iteration were defined as follows:

$$\text{Return } \gamma_T \text{ if } \left\{ \begin{array}{l} \frac{|\gamma_{T,i+1} - \gamma_{T,i}|}{\gamma_{T,i+1}} < 10^{-6} \\ \text{AND} \\ |\mu_I \sin \gamma_I - \mu_{T,i+1} \sin \gamma_{T,i+1}| < 10^{-10} \end{array} \right.$$

Results of this anisotropic and collisionless refraction iteration are presented in Figure 17. From the results, a number of observations can be made. First of all, the initial guess using an isotropic refractive index usually gives refraction angles close to the actual value. The most extreme breakdown of this observation can be seen when an X-wave refracts from free space ($n_1 = 1$), and the initial isotropic refraction angle deviates by almost 10° from the final iterated refraction angle. It must be noted however, that the parameter values used in table 1 demonstrate typical values for a $f \approx 4$ MHz wave propagating in the F_2 layer with a critical frequency of ≈ 2.2 MHz. Hence the refraction from free space directly to the thickest F_2 layer is not realistic, since the refraction is bound to happen gradually through smaller transitions. Nevertheless, this clearly demonstrates the importance of including anisotropy in the refraction calculations, as it can affect the resulting refraction angle significantly.

Furthermore, it can be noted that the iteration converges quite rapidly to the correct refraction angle, and usually the convergence proceeds to adequate precision after just two iteration steps. Moreover, sufficient numeric precision is usually reached after five iterations, while the most extreme refractions still seem to take less than ten iterations. While this may not be completely representative of the

most complicated refraction events that might occur in the finished ray tracer, these results do assure of the applicability of the proposed numeric method in nominal situations.

The 64-bit double-precision floating point data types used in C11 and Matlab are structured to 8 bytes of storage size, resulting in 16 decimal digits according to the IEEE 754 standard [13]. Consequently, lowering the stop condition tolerances to arbitrarily low values will not increase the accuracy of iteration after a certain threshold. The observant reader might notice that the absolute errors given in figure 17 are larger than the specified stop condition tolerance - this discrepancy is most likely caused by the test program not printing all the decimals of the angle. This demonstrates the effects of floating-point representations, and that defining a certain stop condition does not automatically result in the desired iteration precision.

In the next part of the test we decided to study the effects of collisions on the reliability of the pseudo-real ray method, by computing the argument of the refractive index presented in Eq. 3.15. This was done by computing the refractive index n (Eq. 2.24) for a set of realistic extremes of X , Y and Z . The refractive index was then computed for propagation angles θ between 0 and π , and the resulting $-arg(n)$ are presented in Appendix G.

From the graphs in Appendix G, a number of observations must be made. Although the ordinary wave argument is in all tested cases well below the 10° limit, the extraordinary wave refractive index may be almost entirely imaginary in the same situations. Although the most extreme cases represent near-resonance scenarios ($X \approx 1$ or $Y \approx 1$), it is worth noting that while the refractive index can be mostly real for some propagation directions, it may be mostly imaginary in other propagation directions. This has a significant bearing on the proposed pseudo-real ray tracing method. It is hence recommended that the Suomi 100 ray tracer also evaluates the refractive index arguments, and warns the user when the argument becomes too high in order to avoid unrealistic ray paths.

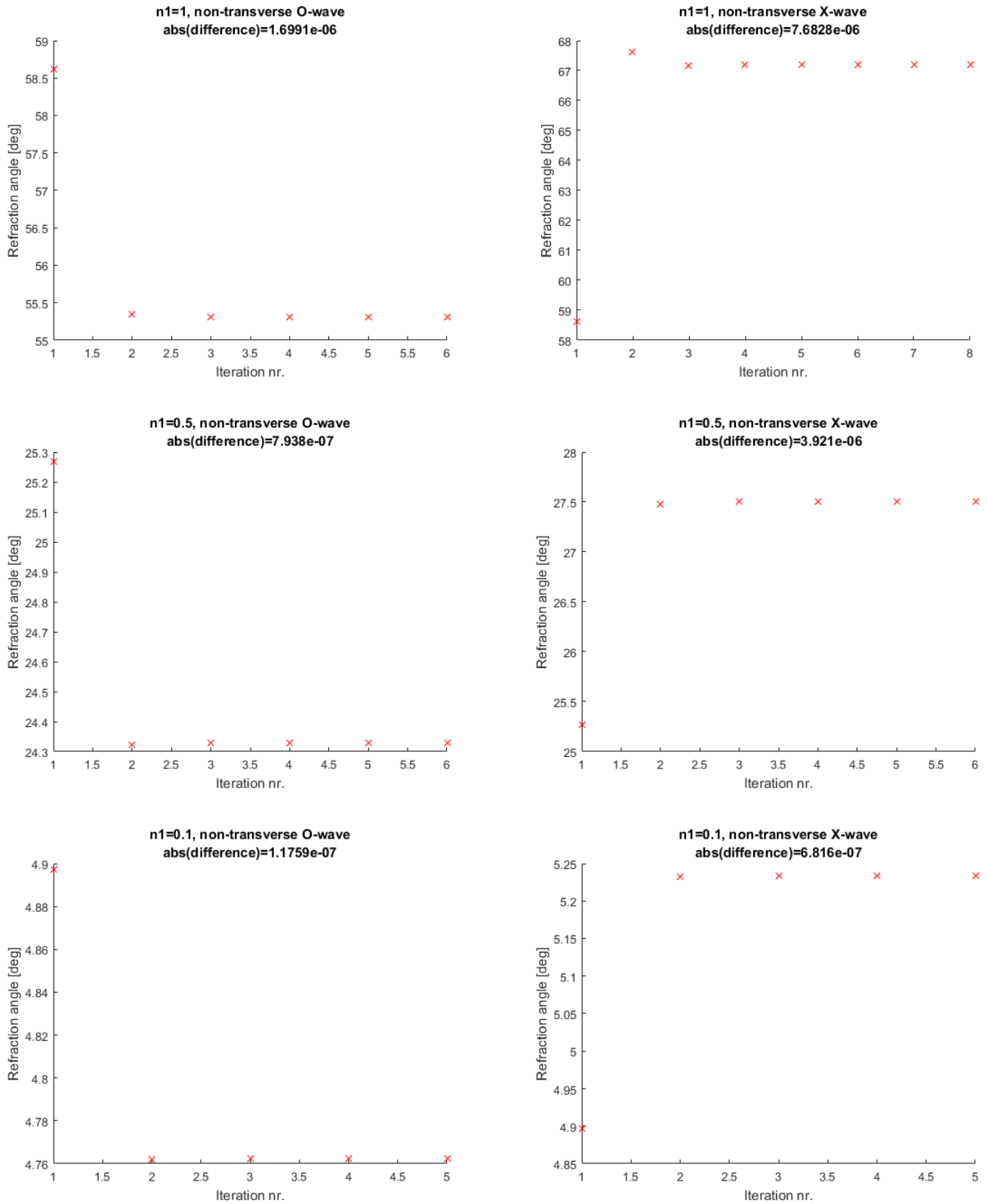


Figure 17: Convergence of the numerical refraction method in an anisotropic and collisionless ionosphere. The horizontal axis presents how many iterations have been needed to evaluate the refraction angle given by the vertical axis. Here abs(difference) denotes the absolute error in Snell's law for the last iterated value (Eq. 3.22).

4.5 Limitations of the numerical method

The numerical pseudo-real Poynting vector method proposed in this report is the result of a number of simplifications that make ray tracing computations simpler and faster, but some of these simplifications may lead to unrealistic ray paths that would not come about in a more general model. In this report, we have done our best to justify the simplifications, and if necessary underline their shortcomings, based on both literary sources and numerical analysis presented in this report. At this point, it is worthwhile to point out some inevitable limitations of the proposed method, so that future versions of the ray tracer may be developed to account for these phenomena.

The term *lateral deviation* refers to the phenomenon of rays being displaced out of the plane of incidence. While our ray tracer does account for this by computing the ray vector direction after refraction using Eqs. 3.29-3.31, the boundary normal is so far simplified as being parallel to the density gradient, resulting in the refracted waves always being in the plane of incidence (defined by the incident wave normal and the density gradient). Anisotropy causes the refractive index gradient $\nabla_{\mathbf{r}}\mu$ to be slightly displaced from the density gradient direction, and accounting for this might introduce more physical ray paths. However, Davies argues in [7] that this effect is quite negligible, although he does not specify the conditions for when the effects may become significant.

Furthermore, it was shown in chapter 4.5 that the pseudo real approximation can break down in ionospheric propagation. To better account for these cases, it might be worth investigating a more general ray tracing method for complex rays. This might for example involve the bilinear concomitant vector presented in chapter 2.4, or may incorporate a Hamiltonian ray tracing treatment (see [6]).

Another simplification employed by the proposed ray tracer, is that it models radio transmissions as consisting of a single constant frequency. In reality, the signal is modulated to consist of a spectrum of frequencies, i.e. a wave packet - for example, an AM signal is usually created by modulating the amplitude of a sinusoidal carrier wave with an input signal. The single frequency approach used by our ray tracer can be interpreted as tracing the carrier wave of operating frequency f . For an overview of wave packets, see [6].

Furthermore, the proposed ray tracer employs a static and relatively smooth ionospheric background. A more realistic time-varying medium inevitably introduces new ray dynamics that is not present in the proposed method. For example, in a time-varying medium the ray frequency changes during propagation [9]. Although modelling the ionosphere as a static background might be justified for nominal radio transmissions, including a dynamic background might prove interesting when studying ray propagation in more 'violent' scenarios, such as geomagnetic storms or other planets.

While the polarisation formulae given in chapter 2.4 allow the evaluation of the electromagnetic field component ratios associated with the propagating wave, the proposed ray tracer is still just that - a ray approximation that does not take into account the ray phase or its field components. A more general full wave method

would allow tracing the field dynamics and its consequences, such as the reflection and transmission coefficients presented in [6] and subsequent signal amplitudes. Fortunately, it is argued in [6] and [24] that full wave methods become necessary only below 1 MHz for terrestrial applications, because the ionospheric background would change considerably within one wavelength for such low ray frequencies. However, if the ray tracer is planned to be utilized for studying radio propagation in other environments (such as any of the other planets in the Solar System), it might be worth considering how a full wave tracer would fare against a more simple ray tracer presented in this report.

5 Summary and discussion

In this report we summarized basic ionospheric ray tracing principles from cold plasma theory, and studied a variety of published computational ray tracing implementations. We concluded that a number of publications on the subject support practical ray path reversibility, suggesting that the prospect of studying global HF/MF transmissions through ray inversion is feasible for the Suomi 100 mission. Furthermore, it was observed that the commercial ray tracing software previously nominated for this purpose, Proplab Pro 3, exhibits inexplicable ray path non-reversibility even in simplified isotropic simulations. Due to the source code of Proplab not being public, the cause of the observed non-reversibility could not be explained, prompting us to develop a ray tracing program of our own.

A majority of this report focuses on elaborating the key principles of the proposed ray tracer. We laid out characteristics of the simulated ionospheric medium, the ray refraction and propagation methodology, a rudimentary software architecture, and implemented a test code written in C11 to analyze the feasibility of our proposed iterative refraction method. We observed that the tried iterative refraction calculations converge in less than ten iterations, and that the resulting refracted wave directions satisfy Snell's law to less than a 10^{-6} absolute error.

We also conducted a brief analysis of the reliability of the proposed pseudo-real ray approach. Ray tracings performed in Proplab with both collisional and non-collisional ionospheres exhibited barely any differences between each other, giving the impression that collisions have at best a very minute effect on ray paths. This conclusion was also found supported by ray tracing theory [6]. It was also decided to study the refractive index argument $-arg(n)$ for some extreme parameter values, and it was observed that the pseudo-real method may break down in some of these scenarios, more prominently for the X-wave than the O-wave.

A great deal of the work was concentrated with distinguishing possible limitations and desirable improvements to the proposed method (see chapter 4.5). The ray tracer methodology presented in this report is at best a 'work in progress', and it must be recognized that some vital properties necessary for a functional ray tracer have barely been touched upon. The most pressing matters in this regard are listed below:

1. 3D grid implementation. The exact solution of how to set up the possible grid cells, and how to recognize ray collisions with the grid cell boundaries, is still an open question. It might even be worth considering to implement a linear interpolation of adjacent grid cells and their corresponding ionospheric quantities, which could possibly enable the ray tracer to propagate the rays in predetermined step lengths and compute refraction parameters anywhere in the domain.
2. Realistic evaluation of collision frequency profiles. In this report, it was briefly stated that the effective collision frequency ν is expected to be of magnitude 10^4 Hz or less, but this conclusion is conspicuously lackluster and of no use if the ray tracer is planned to be utilized in more exotic environments outside

Earth. It is thus imperative, that a more general collision frequency profile is conceived from available ionospheric quantities.

3. Signal attenuation. When the ray refractive index exhibits an imaginary part, the ray amplitude is attenuated. Computing this attenuation along the ray path is necessary, for it would allow the user to recognize paths where evanescent rays practically stop propagating. This can occur even for non-collisional media at cutoff- and resonance conditions, but including a realistic collision profile (see item 2) would allow more accurate tracing ray attenuation. For an overview of wave absorption per unit length, see [7] and [10].
4. Generation of ionospheric profiles without the need to resort to web scraping. In this report, NASA's IRI web tool [28] was scraped to obtain an analysis of the IRI 2012 model, but this provisory method is not feasible for generating an extensive 3D ray tracing grid. If we could execute the IRI 2012 model from our own computers, we would be enabled to rapidly generate a realistic, high-resolution ionospheric background for terrestrial ray tracing. For other environments, the necessity of corresponding ionospheric models is inevitable if we wish to perform ray tracing in these environments.

Once the issues listed above are resolved, the Suomi 100 ray tracer should proceed with testing the results. The ray paths computed by the Suomi 100 ray tracer version 1.0 could for instance be compared to the corresponding results given by Proplab. Code validation is essential for our ray tracing approach, for it must be noted that the methods proposed in this report differ from the Hamiltonian methods employed by a majority of ray tracing algorithms (for example, see [27] and [22]). Once it can be confirmed that our ray tracer demonstrates realistic ray paths, the program can be utilized in the context of the Suomi 100 mission, and possibly other purposes deemed appropriate by the Aalto Space Physics group.

References

- [1] Aalto University Wiki : *hybteam Home*. Referenced 10.8.2016. Available at: <https://wiki.aalto.fi/display/hybteam/hybteam+Home>.
- [2] Altman, C. & Suchy, K. : *Reciprocity, Spatial Mapping and Time Reversal in Electromagnetics*. Kluwer Academic Publishers, 1991.
- [3] The American Radio Relay League (ARRL) : *The ARRL Handbook for Radio Communications*. ARRL, Ninety-Third Edition, 2016.
- [4] Booker, H. : *Application of the Magneto-Ionic Theory to Radio Waves Incident Obliquely Upon a Horizontally Stratified Ionosphere*. Journal of Geophysical Research, Vol.54(3), pp.243-274, September 1949.
- [5] Booker, H. : *Cold Plasma Waves*. Martinus Nijhoff Publishers, 1984.
- [6] Budden, K.G. : *The Propagation of Radio Waves: the Theory of radio waves of low power in the ionosphere and magnetosphere*. Cambridge University Press, 1985.
- [7] Davies, K. : *Ionospheric Radio*. Peter Peregrinus Ltd., 1990.
- [8] Finnish Communications Regulatory Authority: *Frequency Allocation Table*. Referenced 19.7.2016. Available at: <https://www.viestintavirasto.fi/en/spectrum/radiospectrumuse/frequencyallocationtable.html>.
- [9] Fitzpatrick, R. : *Plasma Physics: An Introduction*. CRC Press, Taylor & Francis Group, 2014.
- [10] van Gijlswijk, R. : *A feasibility study on ground-based localization for Mars exploration*. Master's thesis, Aalto University and Luleå University of Technology, 2015.
- [11] Griffiths, D. : *Introduction to Electrodynamics*. Pearson Education, 4th edition, 2013.
- [12] Hunsucker, R. & Hargreaves, J. : *The High-Latitude Ionosphere and its Effects on Radio Propagation*. Cambridge University Press, 2003.
- [13] Institute of Electrical and Electronics Engineers (IEEE) : *754-2008 - IEEE Standard for Floating-Point Arithmetic*. E-ISBN 978-0-7381-5752-8, 2008.
- [14] Kelso, J. : *Radio Ray Propagation in the Ionosphere*. McGraw-Hill, 1964.
- [15] Kivelson, M. & Russell, C. : *Introduction to Space Physics*. Cambridge University Press, 1995.
- [16] Koskinen, H. : *Johdatus plasmafysiikkaan ja sen avaruussovellutuksiin*. Limes, 2nd edition, 2011.

- [17] National Aeronautics and Space Administration (NASA) : *International Reference Ionosphere*. Referenced 3.8.2016. Available at: <http://iri.gsfc.nasa.gov/>.
- [18] National Aeronautics and Space Administration (NASA) : *Representation of Earth's Invisible Magnetic Field*. Referenced 10.8.2016. Available at: http://www.nasa.gov/mission_pages/sunearth/news/gallery/Earths-magneticfieldlines-dipole.html.
- [19] National Oceanic and Atmospheric Administration (NOAA) : *The US/UK World Magnetic Model for 2015-2020*. Referenced 3.8.2016. Available at: <https://www.ngdc.noaa.gov/geomag/WMM/DoDWMM.shtml>.
- [20] Pitkäranta, J.: *TKK:n Laaja matematiikka 1*. Books on Demand (self-published), 2012.
- [21] Pitkäranta, J.: *TKK:n Laaja matematiikka 2*. Books on Demand (self-published), 2013.
- [22] Reilly, M. : *Efficient ray tracing through a realistic ionosphere*. Radio Science, Volume 23, Number 3, May-June 1988.
- [23] Schunk, R. & Nagy, A. : *Ionospheres*. Cambridge University Press, 2nd edition, 2009.
- [24] Smith, M.S. : *Non-reversibility for radio rays in the ionosphere*. Journal of Atmospheric Physics and Terrestrial Physics, Vol. 38, pp. 37 to 44, 1976.
- [25] Solar Terrestrial Dispatch : *Proplab Pro version 3*. Referenced 4.8.2016. Available at: <http://www.spacew.com/www/proplab.html>.
- [26] Sparr, G. & Sparr, A. : *Kontinuerliga system*. Studentlitteratur AB, 2012.
- [27] Tsai, L.-C. et al. : *Three-dimensional numerical ray tracing on a phenomenological ionospheric model*. Radio Science, Volume 45, Issue 5, October 2010.
- [28] Virtual Ionosphere, Thermosphere, Mesosphere Observatory (VITMO): *International Reference Ionosphere - IRI-2012* . Web tool for computing IRI parameters. Referenced 29.7.2016. Available at: http://omniweb.gsfc.nasa.gov/vitmo/iri2012_vitmo.html.

A Cartesian coordinate linear transformations

In order to perform the planar refraction computations (chapter 3.6) and to visualize vectors in a simple frame, it is convenient to perform a linear transformation of Cartesian vectors \mathbf{x} into the desired frame \mathbf{x}' . The transformations are defined by a corresponding (3×3) linear transformation matrix \mathbf{A}

$$\mathbf{x}' = \mathbf{A}\mathbf{x} \quad (\text{A.1})$$

where the vectors \mathbf{x}' and \mathbf{x} are evaluated in a proper Cartesian frame, e.g.

$$\mathbf{x} = a_x \hat{e}_x + a_y \hat{e}_y + a_z \hat{e}_z. \quad (\text{A.2})$$

A.1 To plane of incidence

The plane of incidence is defined by the incident wave normal \mathbf{k} and the boundary unit normal $\mathbf{s} \equiv \frac{\nabla N}{|\nabla N|}$, defined in an arbitrary Cartesian frame \mathbf{x} . For this transformation, \mathbf{s} is in the positive $\hat{e}_{z'}$ -direction and $\hat{e}_{y'}$ is normal to the plane:

- the z-axis is in the direction of \mathbf{s} , i.e. $\hat{e}_{z'} = \mathbf{s}$
- the incident wave normal \mathbf{k}_I lies in the $(x'-z')$ -plane, i.e. $\hat{e}_{y'} = \frac{\mathbf{k} \times \mathbf{s}}{|\mathbf{k} \times \mathbf{s}|}$
- the x-axis is subsequently $\hat{e}_{x'} = \hat{e}_{y'} \times \hat{e}_{z'}$

We wish to select the boundary normal direction which points away from the incident side of the boundary. In the MatRay code developed in this work, this is done by a logical operation:

$$\begin{aligned} \gamma_I &= \arccos \frac{\mathbf{k} \cdot \nabla N}{|\mathbf{k}| |\nabla N|} \\ \text{IF}(\gamma_I > \frac{\pi}{2}) : \\ &\quad \nabla N \rightarrow (-\nabla N) \\ \gamma_I &= \arccos \frac{\mathbf{k} \cdot \nabla N}{|\mathbf{k}| |\nabla N|} \end{aligned}$$

The transformation matrix is thus given by A.3, which transforms a vector into the plane of incidence system:

$$\frac{1}{b} \begin{bmatrix} s_z(s_z k_x - s_x k_z) - s_y(s_x k_y - s_y k_x) & s_x(s_x k_y - s_y k_x) - s_z(s_y k_z - s_z k_y) & s_y(s_y k_z - s_z k_y) - s_x(s_z k_x - s_x k_z) \\ (s_y k_z - s_z k_y) & (s_z k_x - s_x k_z) & (s_x k_y - s_y k_x) \\ b s_x & b s_y & b s_z \end{bmatrix}, \quad (\text{A.3})$$

$$b = |\mathbf{s} \times \mathbf{k}| = \sqrt{(s_y k_z - s_z k_y)^2 + (s_z k_x - s_x k_z)^2 + (s_x k_y - s_y k_x)^2}. \quad (\text{A.4})$$

In the MatRay code, the transformation A.3 is performed by the function `transform_to_planeofincidence`. It must be pointed out, that this transform is not defined in the singular case when \mathbf{s} and \mathbf{k} are parallel, i.e. normal incidence.

However, in this special case no refraction calculations are necessary since the wave passes through the boundary without changing direction, and the transformation A.3 is not needed.

When transforming from the plane system back to the global system, the transformation is given by the inverse matrix of A.3. Since the matrix is orthogonal [21], the inverse transformation is simply the transpose of A.3, given by

$$\frac{1}{b} \begin{bmatrix} s_z(s_z k_x - s_x k_z) - s_y(s_x k_y - s_y k_x) & s_y k_z - s_z k_y & b s_x \\ s_x(s_x k_y - s_y k_x) - s_z(s_y k_z - s_z k_y) & s_z k_x - s_x k_z & b s_y \\ s_y(s_y k_z - s_z k_y) - s_x(s_z k_x - s_x k_z) & s_x k_y - s_y k_x & b s_z \end{bmatrix}. \quad (\text{A.5})$$

In the MatRay code, the inverse transformation A.5 is performed by the function `transform_from_planeofincidence`.

A.2 To propagation coordinates

Although the ray tracer developed in the context of this report does not trace polarisations, it might be of use in future version to investigate the dynamics of the wave eigenvectors, i.e. its electric field and magnetic field vectors. The polarisation equations and the axes presented in chapter 2.4 are chosen in a system for which

- the z-axis is in the direction of wave propagation, i.e. $\hat{e}_{z'} = \frac{\mathbf{k}}{|\mathbf{k}|}$
- the background magnetic field \mathbf{B}_0 lies in the $(x'-z')$ -plane, i.e. $\hat{e}_{y'} = \frac{\mathbf{k} \times \mathbf{B}_0}{|\mathbf{k} \times \mathbf{B}_0|}$
- the x-axis is subsequently $\hat{e}_{x'} = \hat{e}_{y'} \times \hat{e}_{z'}$

These definitions uniquely determine the transformation matrix \mathbf{A} for a vector \mathbf{x} (which components are given in an arbitrary coordinate system) as

$$\frac{1}{ab} \begin{bmatrix} k_z(k_z B_x - k_x B_z) - k_y(k_x B_y - k_y B_x) & k_x(k_x B_y - k_y B_x) - k_z(k_y B_z - k_z B_y) & k_y(k_y B_z - k_z B_y) - k_x(k_z B_x - k_x B_z) \\ a(k_y B_z - k_z B_y) & a(k_z B_x - k_x B_z) & a(k_x B_y - k_y B_x) \\ b k_x & b k_y & b k_z \end{bmatrix}. \quad (\text{A.6})$$

$$a = |\mathbf{k}| = \sqrt{k_x^2 + k_y^2 + k_z^2}, \quad (\text{A.7})$$

$$b = |\mathbf{k} \times \mathbf{B}_0| = \sqrt{(k_y B_z - k_z B_y)^2 + (k_z B_x - k_x B_z)^2 + (k_x B_y - k_y B_x)^2}. \quad (\text{A.8})$$

One must note, that the transformation above is not defined in the singular case $\mathbf{k} \parallel \mathbf{B}_0$. In this case however, the polarisations are strictly transverse, and formulating proper transforms is simple. This is not studied further in this report, but we chose to present this 'propagation transform' for possible future reference.

For transforming back to the global frame, the inverse transformation can be obtained from the transpose of matrix A.6:

$$\begin{bmatrix} \frac{1}{ab}(k_z(k_z B_x - k_x B_z) - k_y(k_x B_y - k_y B_x)) & \frac{1}{b}(k_y B_z - k_z B_y) & \frac{1}{a} k_x \\ \frac{1}{ab}(k_x(k_x B_y - k_y B_x) - k_z(k_y B_z - k_z B_y)) & \frac{1}{b}(k_z B_x - k_x B_z) & \frac{1}{a} k_y \\ \frac{1}{ab}(k_y(k_y B_z - k_z B_y) - k_x(k_z B_x - k_x B_z)) & \frac{1}{b}(k_x B_y - k_y B_x) & \frac{1}{a} k_z \end{bmatrix}. \quad (\text{A.9})$$

A.3 To spherical coordinates

The orthogonal spherical vectors $\hat{\mathbf{r}}$, $\hat{\lambda}$ and $\hat{\psi}$ can be expressed using a set of Cartesian coordinates as [20]

$$\hat{\mathbf{r}} = \cos \lambda \cos \psi \hat{\mathbf{e}}_{\mathbf{x}} + \cos \lambda \sin \psi \hat{\mathbf{e}}_{\mathbf{y}} + \sin \lambda \hat{\mathbf{e}}_{\mathbf{z}}, \quad (\text{A.10})$$

$$\hat{\lambda} = \sin \lambda \cos \psi \hat{\mathbf{e}}_{\mathbf{x}} + \sin \lambda \sin \psi \hat{\mathbf{e}}_{\mathbf{y}} - \cos \lambda \hat{\mathbf{e}}_{\mathbf{z}}, \quad (\text{A.11})$$

$$\hat{\psi} = -\sin \psi \hat{\mathbf{e}}_{\mathbf{x}} + \cos \psi \hat{\mathbf{e}}_{\mathbf{y}}. \quad (\text{A.12})$$

Here λ and ψ are respectively the latitude and longitude, as opposed to the standard convention of using polar and azimuthal angles (see Figure 18). The notation of local

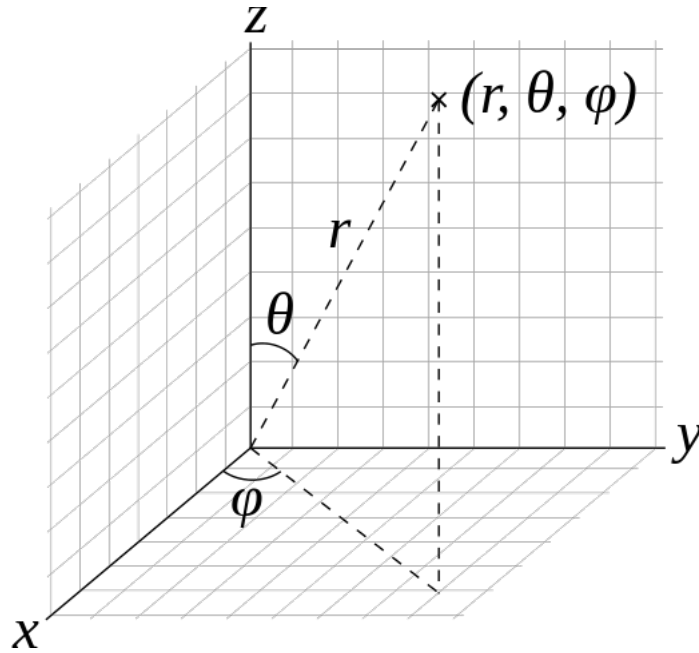


Figure 18: Spherical coordinates as commonly used in physics: radial distance r , polar angle θ and azimuthal angle φ . This convention is not used for the ray tracer's global coordinate system - instead, the latitude λ is given by $\lambda = \frac{\pi}{2} - \theta$. The longitude ψ is still given by $\psi = \varphi$.

spherical altitude and arc coordinates used in this report can be explained as follows (see Figure 19):

- h is the altitude above the Earth's surface directly in the local radial direction
- $\Delta\zeta$ is the displacement in the local North-South direction, parallel to the vector $\hat{\lambda}$, along the arc of the great circle in that direction
- $\Delta\chi$ is the displacement in the local East-West direction, parallel to the vector $\hat{\psi}$, along the arc of the great circle in that direction

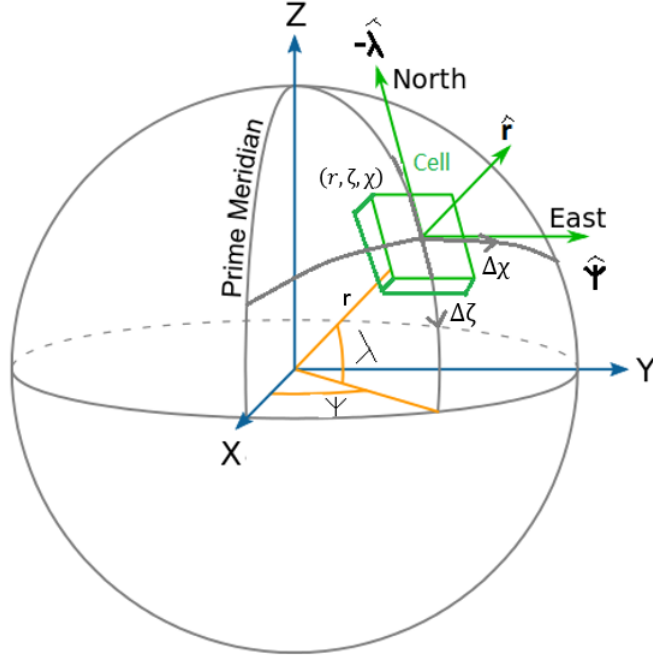


Figure 19: Illustration of the local altitude and arc coordinates. The radial distance r is given by $r = R_E + h$. The grid cell is placed at the position (r, ζ, χ) .

This choice of coordinates is useful for the quasi-rectangular simulation grid, because adjacent grid cells can easily be expressed locally by a discrete amount of displacements in these coordinates. Furthermore, the boundary normal in local spherical coordinates is explicitly expressed by

$$\nabla'_{\mathbf{r}} N = \hat{\mathbf{r}} \frac{\partial N}{\partial h} + \hat{\lambda} \frac{\partial N}{\partial \zeta} + \hat{\psi} \frac{\partial N}{\partial \chi} \quad (\text{A.13})$$

For evaluating the boundary normal in the global coordinate system, one requires the inverse transformation of A.10-A.12. Due to their orthogonality, the inverse transformation is trivially given by the transpose of A.10-A.12, given by matrix A.14:

$$\mathbf{A} = \begin{bmatrix} \cos \lambda \cos \psi & \sin \lambda \cos \psi & -\sin \psi \\ \cos \lambda \sin \psi & \sin \lambda \sin \psi & \cos \psi \\ \sin \lambda & -\cos \lambda & 0 \end{bmatrix}. \quad (\text{A.14})$$

As an example, at the location (60°N, 20°W) some altitude h above the ground, the local density gradient is evaluated from equations 3.7-3.9 to be

$$\nabla'_{\mathbf{r}} N = 2.0 \hat{\mathbf{r}} - 0.1 \hat{\lambda} + 0.3 \hat{\psi} \text{ m}^{-4}. \quad (\text{A.15})$$

For this geographic location, the inverse transformation matrix A.14 is given by

$$\mathbf{A} = \begin{bmatrix} \cos(60^\circ) \cos(-20^\circ) & \sin(60^\circ) \cos(-20^\circ) & -\sin(-20^\circ) \\ \cos(60^\circ) \sin(-20^\circ) & \sin(60^\circ) \sin(-20^\circ) & \cos(-20^\circ) \\ \sin(60^\circ) & -\cos(60^\circ) & 0 \end{bmatrix} \quad (\text{A.16})$$

$$\approx \begin{bmatrix} 0.470 & 0.814 & 0.342 \\ -0.171 & -0.296 & 0.937 \\ 0.866 & -0.5 & 0 \end{bmatrix}. \quad (\text{A.17})$$

Hence, the density gradient in the global coordinate system is given by

$$\nabla_{\mathbf{r}} N = \mathbf{A} \nabla'_{\mathbf{r}} N \quad (\text{A.18})$$

$$\approx 0.961 \hat{e}_{\mathbf{x}} - 0.0313 \hat{e}_{\mathbf{y}} + 1.78 \hat{e}_{\mathbf{z}} \text{ m}^{-4}. \quad (\text{A.19})$$

B Alternative method for transforming refracted wave normals to the global system

After refraction, it is convenient to transform the wave vector from the incident plane system back to the original system using matrix A.5. Since the refracted wave still lies in the plane of incidence in this simplified ray tracer, a transform for the refracted wave can easily be conceived by solving a linear system. The proposed program will use the results presented in Appendix A.1 since the transformations are exact, but we still chose to present an alternative method due to its simplicity.

The program has to be provided with \mathbf{s} , \mathbf{k} , γ_I , and γ_T or γ_R depending on whether transmission or reflection is traced (see Figure 9 for how the angles are defined). All angles are between 0 and $\frac{\pi}{2}$. Before refraction is performed, the boundary normal pointing away from the incident side of the boundary has been selected (Appendix A.1). For this analysis however, it is necessary that the selected boundary normal points into the same side of the boundary as the refracted wave. For instance, for a reflected wave one must use the boundary normal pointing into the incident side. This selection is done by a logical operation:

IF(*Reflect*) :

$$\nabla N \rightarrow (-\nabla N)$$

ELSE:

∇N is unchanged

The equations also look different for the transmitted and reflected case, hence the program would be branched into one of two methods: B.1 for a transmitted wave, and B.2 for a reflected wave.

B.1 Transmitted wave

In the plane of incidence, the transmitted wave unit vector \mathbf{t} can be expressed as a linear combination of the boundary normal \mathbf{s} and the incident wave normal \mathbf{k} , both

of which are defined in the global (original) coordinate system. This defines three scalar linear equations:

$$\mathbf{t} = a\mathbf{s} + b\mathbf{k}. \quad (\text{B.1})$$

Furthermore, the transmitted wave \mathbf{k}_T makes an angle γ_T with the boundary normal, and an angle $\gamma_I - \gamma_T$ with the incident wave $\mathbf{k}_I \equiv \mathbf{k}$. This defines two linear equations:

$$\mathbf{t} \cdot \mathbf{s} = |\mathbf{s}| \cos \gamma_T, \quad (\text{B.2})$$

$$\mathbf{t} \cdot \mathbf{k} = |\mathbf{k}| \cos (\gamma_I - \gamma_T). \quad (\text{B.3})$$

Solving these five linear equations yields a unique solution for the transmitted wave in the global system:

$$t_x = \left(\frac{\sin \gamma_T}{\sin \gamma_I} \right) \frac{k_x}{|\mathbf{k}|} + \left(\cos \gamma_T - \frac{\sin \gamma_T}{\tan \gamma_I} \right) \frac{s_x}{|\mathbf{s}|}, \quad (\text{B.4})$$

$$t_y = \left(\frac{\sin \gamma_T}{\sin \gamma_I} \right) \frac{k_y}{|\mathbf{k}|} + \left(\cos \gamma_T - \frac{\sin \gamma_T}{\tan \gamma_I} \right) \frac{s_y}{|\mathbf{s}|}, \quad (\text{B.5})$$

$$t_z = \left(\frac{\sin \gamma_T}{\sin \gamma_I} \right) \frac{k_z}{|\mathbf{k}|} + \left(\cos \gamma_T - \frac{\sin \gamma_T}{\tan \gamma_I} \right) \frac{s_z}{|\mathbf{s}|}. \quad (\text{B.6})$$

B.2 Reflected wave

In the plane of incidence, the reflected wave unit vector \mathbf{r} can be expressed as a linear combination of the boundary normal \mathbf{s} and the incident wave normal \mathbf{k} , both of which are defined in the global (original) coordinate system. This again defines three scalar linear equations:

$$\mathbf{r} = a\mathbf{s} + b\mathbf{k} \quad (\text{B.7})$$

Furthermore, the reflected wave makes an angle γ_R with the boundary normal (which now points into the incident side of the boundary), and an angle $(\pi - \gamma_I - \gamma_R)$ with the incident wave (see Figure 20). This defines two linear equations:

$$\mathbf{r} \cdot \mathbf{s} = |\mathbf{s}| \cos \gamma_R, \quad (\text{B.8})$$

$$\mathbf{r} \cdot \mathbf{k} = -|\mathbf{k}| \cos (\gamma_I + \gamma_R). \quad (\text{B.9})$$

Solving these five linear equations yields a unique solution for the reflected wave in the global system:

$$r_x = \left(\frac{\sin \gamma_R}{\sin \gamma_I} \right) \frac{k_x}{|\mathbf{k}|} + \left(\cos \gamma_R + \frac{\sin \gamma_R}{\tan \gamma_I} \right) \frac{s_x}{|\mathbf{s}|}, \quad (\text{B.10})$$

$$r_y = \left(\frac{\sin \gamma_R}{\sin \gamma_I} \right) \frac{k_y}{|\mathbf{k}|} + \left(\cos \gamma_R + \frac{\sin \gamma_R}{\tan \gamma_I} \right) \frac{s_y}{|\mathbf{s}|}, \quad (\text{B.11})$$

$$r_z = \left(\frac{\sin \gamma_R}{\sin \gamma_I} \right) \frac{k_z}{|\mathbf{k}|} + \left(\cos \gamma_R + \frac{\sin \gamma_R}{\tan \gamma_I} \right) \frac{s_z}{|\mathbf{s}|}. \quad (\text{B.12})$$

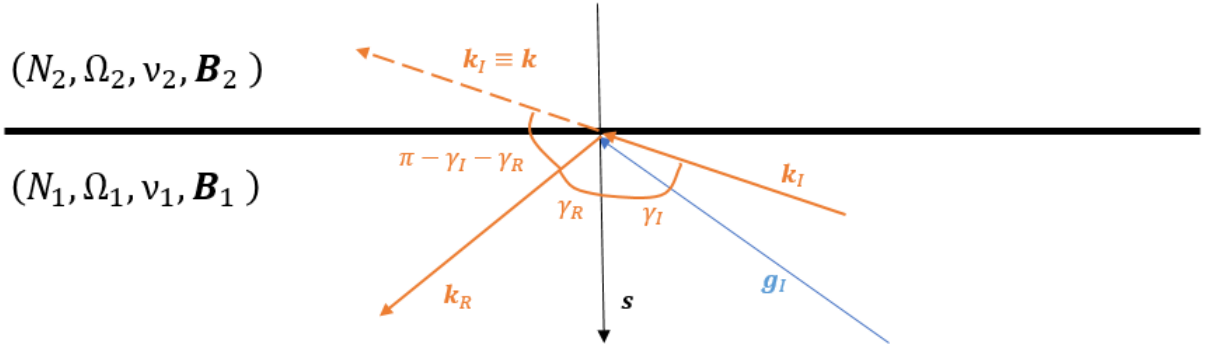


Figure 20: Illustration of a reflected wave after refraction.

C Ray unit vector

From Equation 2.39 one can determine the angle between the wave normal and the ray. The ray unit vector \mathbf{g} lies in the plane defined by the wave normal \mathbf{k} and the magnetic background \mathbf{B}_0 , and the ray can thus be expressed as a linear combination of the two:

$$\mathbf{g} = a\mathbf{k} + b\mathbf{B}_0. \quad (\text{C.1})$$

Furthermore, the ray makes an angle α with the wave normal \mathbf{k} and an angle $(\theta - \alpha)$ with the magnetic background, where θ is the angle between \mathbf{k} and \mathbf{B}_0 :

$$\mathbf{g} \cdot \mathbf{k} = |\mathbf{k}| \cos \alpha, \quad (\text{C.2})$$

$$\mathbf{g} \cdot \mathbf{B}_0 = |\mathbf{B}_0| \cos(\theta - \alpha). \quad (\text{C.3})$$

Solving the linear system defined by these five linear scalar equations yields a unique solution for \mathbf{g} . The solution can be simplified to obtain:

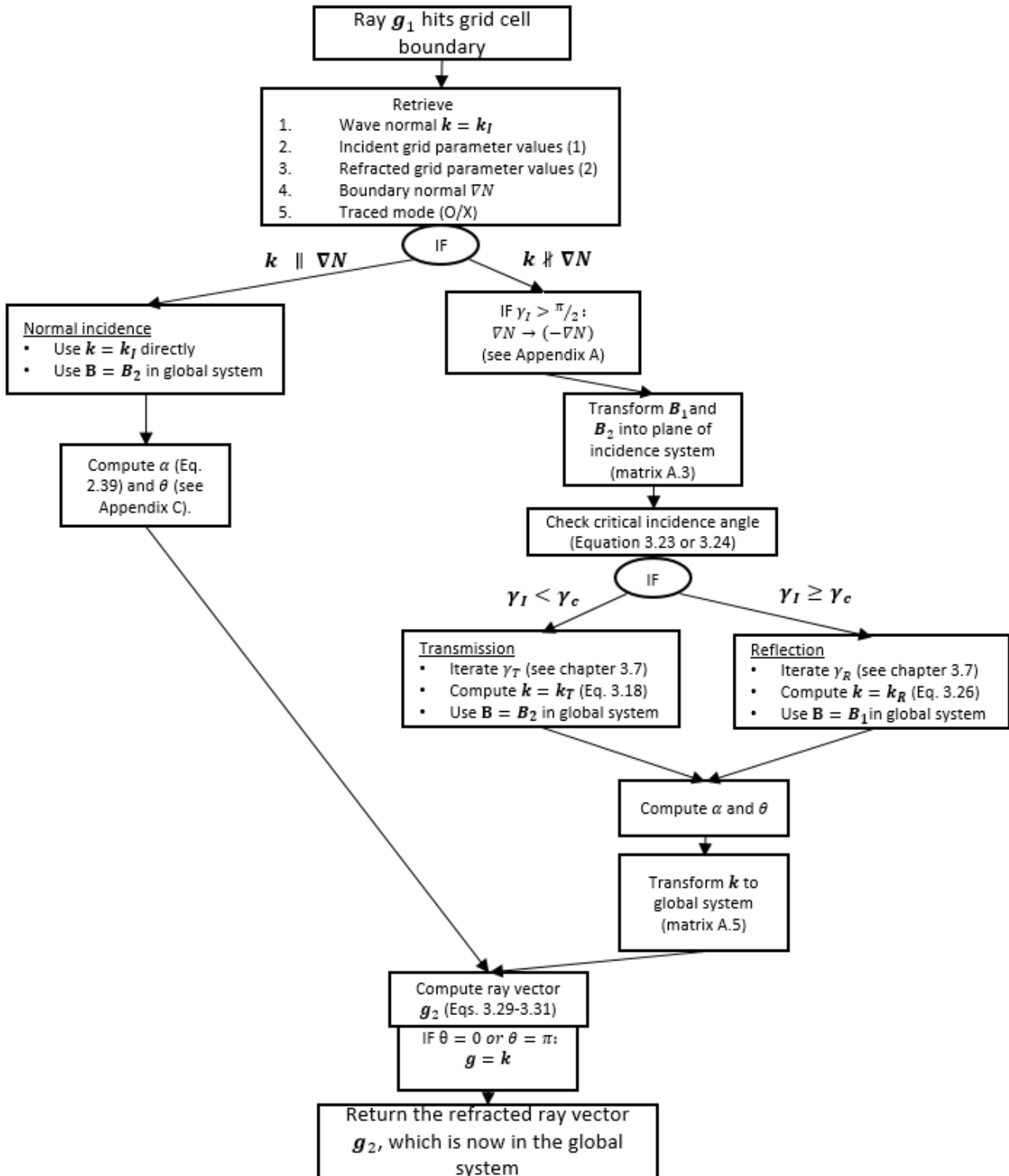
$$g_x = \left(\frac{\sin \alpha}{\sin \theta} \right) \frac{B_x}{|\mathbf{B}_0|} + \left(\cos \alpha - \frac{\sin \alpha}{\tan \theta} \right) \frac{k_x}{|\mathbf{k}|}, \quad (\text{C.4})$$

$$g_y = \left(\frac{\sin \alpha}{\sin \theta} \right) \frac{B_y}{|\mathbf{B}_0|} + \left(\cos \alpha - \frac{\sin \alpha}{\tan \theta} \right) \frac{k_y}{|\mathbf{k}|}, \quad (\text{C.5})$$

$$g_z = \left(\frac{\sin \alpha}{\sin \theta} \right) \frac{B_z}{|\mathbf{B}_0|} + \left(\cos \alpha - \frac{\sin \alpha}{\tan \theta} \right) \frac{k_z}{|\mathbf{k}|}. \quad (\text{C.6})$$

In the special cases $\theta = 0$, $\theta = \pi$ or $|\mathbf{B}_0| = 0$ the ray is in the same direction as \mathbf{k} . These three special cases need to be programmed separately into the ray tracer, as the ray direction equations presented in this chapter would diverge if direct evaluation is performed.

D Flow chart of the ray refraction algorithm



E Multipole expansion of current loop magnetic field

For a static current distribution, the magnetic field is related to the source current by Maxwell's equations

$$\nabla \cdot \mathbf{B} = 0, \quad (\text{E.1})$$

$$\nabla \times \mathbf{B} = \mu_0 \mathbf{j}. \quad (\text{E.2})$$

Equation E.1 ensures the existence of the vector potential \mathbf{A} , which is related to the physical magnetic field by the partial differential equation

$$\mathbf{B} = \nabla \times \mathbf{A}. \quad (\text{E.3})$$

Inserting E.3 into E.2, and employing the Coulomb gauge

$$\nabla \cdot \mathbf{A} = 0 \quad (\text{E.4})$$

gives a Poisson equation for the magnetic vector potential

$$\nabla^2 \mathbf{A} = -\mu_0 \mathbf{j}. \quad (\text{E.5})$$

If the source current \mathbf{j} does not extend to infinity (which is expected for a physical field) a solution to E.5 is given by the Newtonian potential [26]:

$$\mathbf{A}(\mathbf{r}) = \frac{\mu_0}{4\pi} \int \frac{\mathbf{j}}{|\mathbf{r} - \mathbf{r}'|} dV'. \quad (\text{E.6})$$

Here \mathbf{r} denotes the position of measurement, and the primed quantities \mathbf{r}' and dV' respectively the source position and volume element. For an ideally thin current loop carrying the uniform line current I , the current distribution can be expressed by the line element $d\mathbf{l}'$ as

$$\mathbf{j}dV' = I d\mathbf{l}'. \quad (\text{E.7})$$

Inserting E.7 into E.6 gives the more usable form of the vector potential:

$$\mathbf{A}(\mathbf{r}) = \frac{\mu_0 I}{4\pi} \oint \frac{d\mathbf{l}'}{|\mathbf{r} - \mathbf{r}'|}. \quad (\text{E.8})$$

The length $|\mathbf{r} - \mathbf{r}'|$ can be rewritten using the law of cosines

$$\frac{1}{|\mathbf{r} - \mathbf{r}'|} = \frac{1}{\sqrt{r^2 + r'^2 - 2rr' \cos \phi}} \quad (\text{E.9})$$

which can further be written as a Legendre polynomial series expansion

$$\frac{1}{\sqrt{r^2 + r'^2 - 2rr' \cos \phi}} = \sum_{n=0}^{\infty} \frac{1}{r^{n+1}} P_n(\cos \phi) (r')^n. \quad (\text{E.10})$$

Thus, the vector potential can be expressed (exactly) by the multipole expansion

$$\mathbf{A}(\mathbf{r}) = \frac{\mu_0 I}{4\pi} \sum_{n=0}^{\infty} \frac{1}{r^{n+1}} \oint P_n(\cos \phi) (r')^n d\mathbf{l}'. \quad (\text{E.11})$$

The monopole term of E.11 is given by $n = 0$, for which $P_0(\cos \phi) = 1$:

$$\mathbf{A}_0 = \frac{\mu_0 I}{4\pi r} \oint d\mathbf{l}' = 0. \quad (\text{E.12})$$

The monopole term is thus zero everywhere. The all-important dipole term is given by $n = 1$, $P_1(\cos \phi) = \cos \phi$:

$$\mathbf{A}_1 = \frac{\mu_0 I}{4\pi r^2} \oint r' \cos \phi d\mathbf{l}' \quad (\text{E.13})$$

$$= \frac{\mu_0 I}{4\pi r^2} \oint (\mathbf{r}' \cdot \hat{\mathbf{r}}) d\mathbf{l}'. \quad (\text{E.14})$$

The magnetic dipole moment \mathbf{m} is defined as

$$\mathbf{m} = I \oint \mathbf{r}' \times d\mathbf{l}'. \quad (\text{E.15})$$

By using simple vector calculus, it can be shown that for a loop current

$$\mathbf{m} \times \mathbf{r} = Ir \oint (\mathbf{r}' \cdot \hat{\mathbf{r}}) d\mathbf{l}'. \quad (\text{E.16})$$

Inserting E.16 into the dipole term E.14 gives the closed-form expression

$$\mathbf{A}_1 = \frac{\mu_0}{4\pi r^3} (\mathbf{m} \times \mathbf{r}). \quad (\text{E.17})$$

When one is very far away from the current loop, i.e. ($r \gg r'$), the exact solution for the entire vector potential is given by the dipole term E.17. Furthermore, for an ideal current loop of zero size but finite dipole moment, it can be shown that E.17 gives the exact solution everywhere. If we intend to model the geomagnetic field using a small current loop source placed at the center of the Earth, the dipole field gives the field above the surface to very good approximation. It is however completely possible to include higher terms of the multipole expansion (quadrupole, octopole etc.) in the vector potential. This possibility is not analysed further in this report. For an elaborate treatment of the vector potential and multipole expansions, see [11].

The approximate magnetic field of a current loop is then given by inserting E.17 into E.3, producing the dipole magnetic field

$$\mathbf{B}(\mathbf{r}) \approx \nabla \times \mathbf{A}_1 \quad (\text{E.18})$$

$$= \frac{\mu_0 |\mathbf{m}|}{4\pi r^3} [3(\hat{\mathbf{m}} \cdot \hat{\mathbf{r}}) \hat{\mathbf{r}} - \hat{\mathbf{m}}]. \quad (\text{E.19})$$

F Refractive index argument

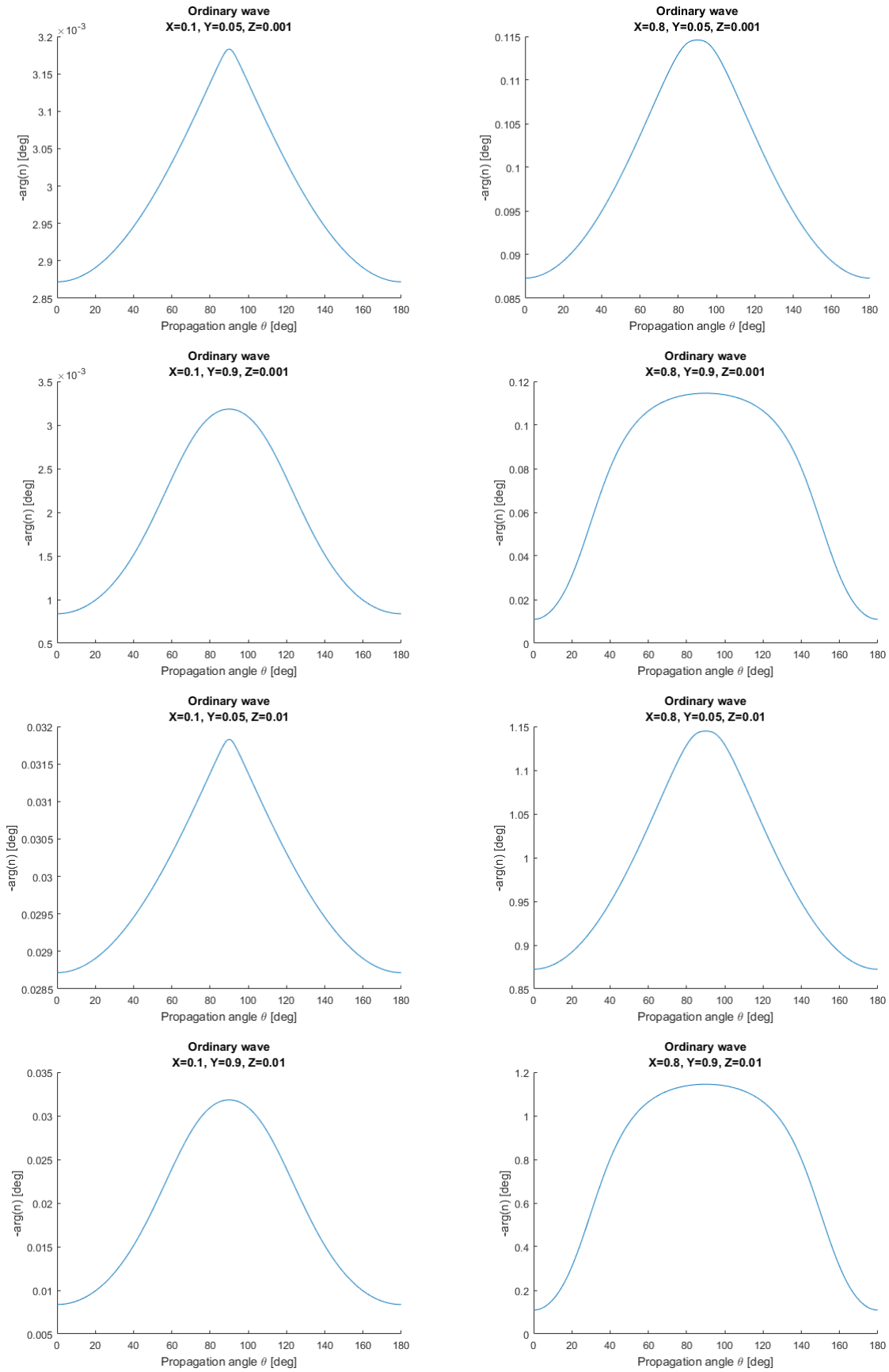


Figure 21: Computed refractive index arguments (Eq. 3.15) for the ordinary wave in some extreme cases. The propagation angle θ is the angle between the wave normal \mathbf{k} and the magnetic background \mathbf{B}_0 .

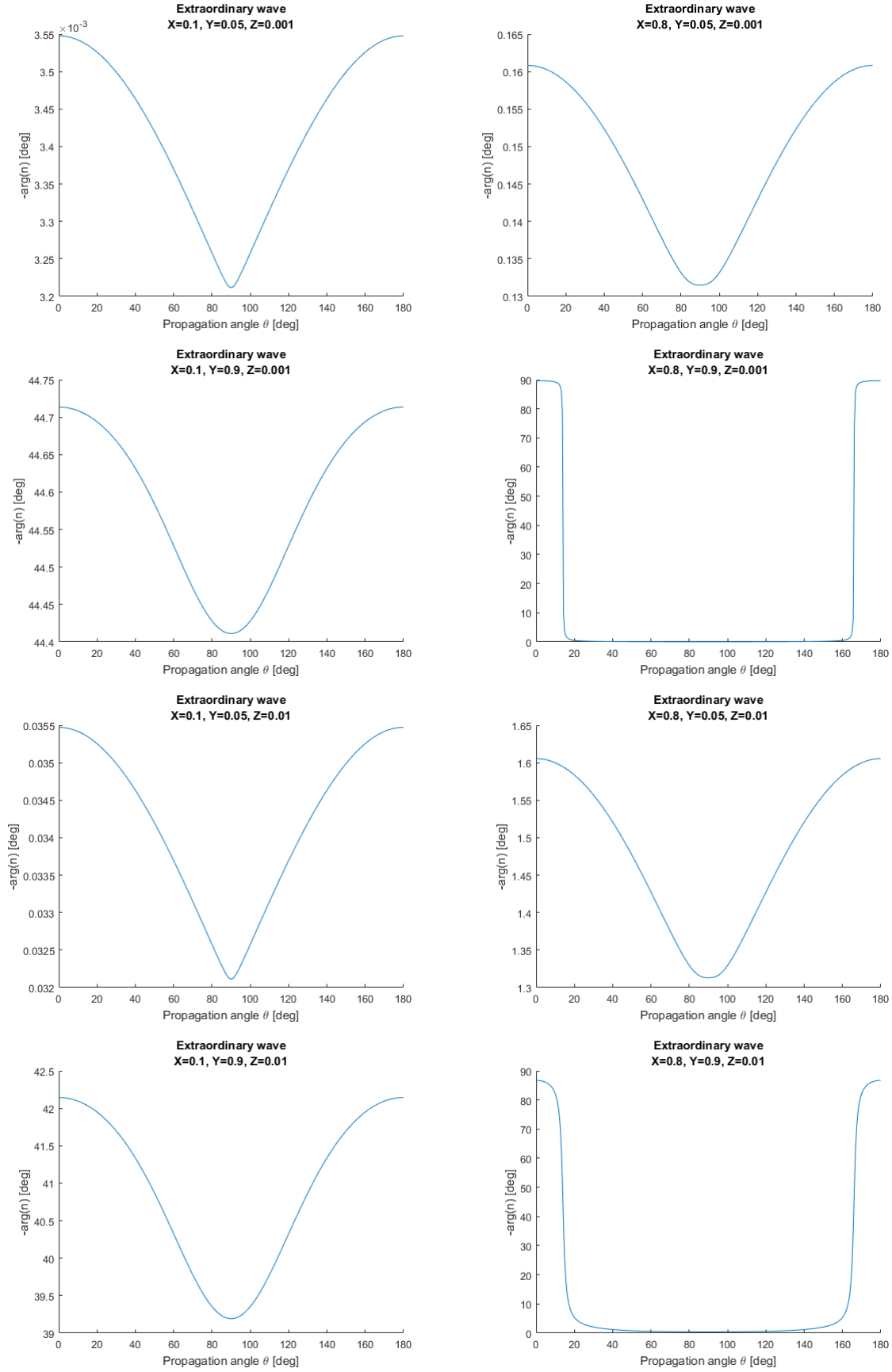


Figure 22: Computed refractive index arguments (Eq. 3.15) for the extraordinary wave in some extreme cases. The propagation angle θ is the angle between the wave normal \mathbf{k} and the magnetic background \mathbf{B}_0 .